Title

Multiferroic Antennas for Use in Biomedical Applications

Permalink

https://escholarship.org/uc/item/29h67006

Author

Burnside, Emily

Publication Date

2023

Peer reviewed|Thesis/dissertation

UNIVERSITY OF CALIFORNIA

Los Angeles

Multiferroic Antennas for Use in Biomedical Applications

A dissertation submitted in partial satisfaction of the requirements for the degree Doctor of

Philosophy in Mechanical Engineering

by

Emily Ailene Burnside

2023

ABSTRACT OF DISSERTATION

Multiferroic Antennas for Use in Biomedical Applications

by

Emily Ailene Burnside

Doctor of Philosophy in Mechanical Engineering

University of California, Los Angeles, 2023

Professor Gregory P. Carman, Chair

While there is a need for low frequency (30-300 kHz) communication through lossy media like seawater and the human body, these dielectric cluttered environments present challenges to conventional communication devices in the form of signal attenuation. This is due to the interaction of the electric field component of electromagnetic radiation with the conductive portions of the surrounding media. Magnetoelectric antennas provide a solution to this problem in that they primarily output magnetic energy in the near field. Furthermore, by using strain-driven magnetoelectric antennas, antenna miniaturization is realizable by operating at acoustic resonance rather than electromagnetic resonance. While there have been successful experimental demonstrations of low frequency magnetoelectric antennas, the community lacks a systematic approach for antenna design and characterization.

This first half of this work presents a decoupled system of models including a method for predicting magnetic moments of bulk samples using Landau-Lifshitz-Gilbert micromagnetic simulations, enabling radiation predictions via an analytical dipole model, resulting in a paradigm shift from dipole radiation validations to dipole radiation predictions. This work includes a

methodical testing approach to assess the antenna's performance in terms of signal strength, quality factor, and radiation patterns, determining the antenna to be comparable to state-of-the-art pacemaker antennas.

The second half of this work discusses the design and characterization of a Galfenol antenna which resonates at two distinct frequencies. This second antenna, called a dual band magnetoelectric antenna, allows for communication via frequency shift keying (FSK) and is the first magnetoelectric to accomplish FSK at two resonance frequencies. This work demonstrates that the data bandwidth can be increased by an order of magnitude and discusses potential for future improvement in data bandwidth.

This dissertation also features a discussion on parasitic effects and mitigation techniques as well as material parametric studies for improved antenna performance. This work presents a comprehensive procedural guide for the design, fabrication, and characterization of low frequency magnetoelectric antennas, effectively bridging a gap in the existing literature.

This dissertation of Emily Ailene Burnside is approved.

Robert N. Candler

Yen-Chih Lin

Yuanxun Wang

Gregory P. Carman, Committee Chair

University of California, Los Angeles

2023

Table of Contents

List of Figures

List of Tables

Acknowledgements

Vita

EDUCATION

University of California, Los Angeles

- Candidate for Doctor of Philosophy in Mechanical Engineering   Expected September 2023

- Master of Science in Mechanical Engineering   March 2022

California Polytechnic State University, San Luis Obispo

- Bachelor of Science Degree in Mechanical Engineering   June 2019

SELECTED PRESENTATIONS AND AWARDS

- March 2022: Oral presentation at SPIE Smart Structures + NDE Symposium, "Experimental demonstration of a multiferroic antenna for use in biomedical applications"

- February 2022: Oral presentation at TANMS-hosted Annual Research Strategy Meeting, "Multiferroic Antenna for Biomedical Applications"

- September 2019: Awarded UCLA Eugene v. Cota-Robles doctoral fellowship, TANMS ERC doctoral fellowship

JOURNAL PUBLICATIONS

- Burnside, E., Tiwari, S., Burnside, S., Candler, R., Henderson, R., Grimm, S., Carman, G. (2023). *An Axial Mode Magnetoelectric Antenna: Radiation Predictions via Multiphysics Modeling with Experimental Validations*. [Manuscript submitted for publication].

- Burnside, E., Burnside, S., Candler, R., Carman, G. (2023) *Experimental Demonstration of Dual Band Multiferroic Antenna for FSK Communication*. [Manuscript in preparation].

- Acosta, A., Burnside, E., Fitzell, K., Carman, G., Chang, J. (In press). Multilayering FeGa with NiFe and Al2O3 to enhance the soft magnetic properties. *Applied Physics Letters.*

Chapter 1: Background and History

1.1 Introduction

Since their creation in the late 1800's, antennas have become increasingly important in our everyday lives. There are countless examples of antennas being implemented into modern technology with relative ease; however, there are still application spaces which present challenges to the successful implementation of antennas. Two such application spaces are the aerospace industry and the biomedical industry. In the aerospace industry, there is a desire to have conformal antennas to reduce visibility and drag on vehicles, while there is an increasing interest in antennas capable of communicating through lossy media such as ocean water. Similarly, antennas in implanted medical devices must be able to communicate through a dielectric cluttered environment for there to be communication through the human body. This, along with size constraints, has led to a push in the biomedical industry for small communication devices capable of communication in lossy media.

Conventional antennas are currently unable to meet these needs for a number of reasons. First, the size of current-based devices such as loop antennas or coils for inductive coupling cannot be significantly decreased without increasing the effects of Joule heating dramatically. Second, conventional antennas must be proportional to the electromagnetic wavelength, meaning that low frequency, large wavelength devices must be large in size. Multiferroic antennas can overcome these size issues; they rely on electric fields rather than currents, so Joule heating is not a concern. They also rely on acoustic resonance instead of electromagnetic resonance, meaning that they can easily be made at smaller sizes.

Multiferroic antennas can also be designed to propagate through lossy media as well because they can be designed to primarily output magnetic fields in the near field. Unlike electric fields, these magnetic fields will not interact with the dielectric cluttered environment. This is important for a number of reasons. Electric field interaction with human tissues presents a safety issue and can lead to adverse side effects in patients like tissue heating or even disorientation, so there is an obvious benefit of using magnetic fields. For antennas operating in the ocean, the electric fields would interact with the saltwater leading to massive attenuation of the signals. Using magnetic based multiferroic antennas are an excellent solution to this issue in that the magnetic fields will not interact with saltwater.

This document describes how multiferroic antennas work and their benefits specifically in the biomedical field through first describing the background and basic science of multiferroic materials and technology. This will be followed by a brief overview of multiferroic applications including memory devices, cell sorting applications, and RF devices, with an emphasis on the latter. A discussion on low frequency multiferroic antennas will follow as this is the most promising solution to the biomedical communication problem. There is work currently being done in the biomedical communication and wireless power transfer space, which will be described in this document. To conclude, I will be presenting the reader with a proposed communication device for use in leadless pacemakers: an axial-extension mode magnetic-based multiferroic antenna.

1.2 Ferromagnetism

Ferroic materials are materials which exhibit a ferroic order. This really refers to the spontaneous breaking of a crystal's symmetry or change in phase [1]. The term "ferroic" could refer to a number

of materials including ferromagnetic and ferroelectric materials. A ferromagnetic material exhibits spontaneous magnetization. V.K. Wadhawan, author of. "Ferroic Materials: A Primer", had a wonderful example of ferromagnetism. They described heating an iron crystal, then cooling it. Upon cooling, the iron crystal has a nonzero magnetic moment in the absence of an external field. This remanent magnetization can be considered the crystal's spontaneous magnetization [1].

1.2.1 Origin of Magnetism

To understand the origins of magnetism, one should have an understanding of Maxwell's equations:

$$\nabla \cdot \vec{D} = \rho \tag{1.1}$$

$$\nabla \cdot \vec{B} = 0 \tag{1.2}$$

$$\nabla \times \vec{E} = -\frac{d\vec{B}}{dt} \tag{1.3}$$

$$\nabla \times \vec{H} = \vec{J} + \frac{d\vec{D}}{dt} \tag{1.4}$$

These equations were first compiled and published in 1865 by James Clerk Maxwell [2] and consist of two versions of Gauss' laws, Equations 1.1 and 1.2, which describe static conditions. Equation 1.3 is Faraday's law which describes the formation of electric fields from time varying magnetic fields. Ampere's law, Equation 1.4, states that moving charges, or a current density, will induce time varying magnetic fields.

We can apply Ampere's law to two cases when discussing the origin of magnetism. One may be familiar with solenoids or current-carrying wires: if you were to run a current through a wire, you could expect a magnetic field to form around it as seen in Figure 1.1a. Note that the direction of

the magnetic field around the wire would be in accordance with the right-hand rule. Now that we have looked at a microscale view of how Ampere's law works, we can zoom in on a considerably smaller example: atoms and their electrons. It is widely known that electrons orbit around the nucleus while simultaneously spinning around their own axis. These two rotational motions act as tiny current loops, each contributing to a sample's total magnetic moment. An entire stack of these electron current loops is shown in Figure 1.1b.
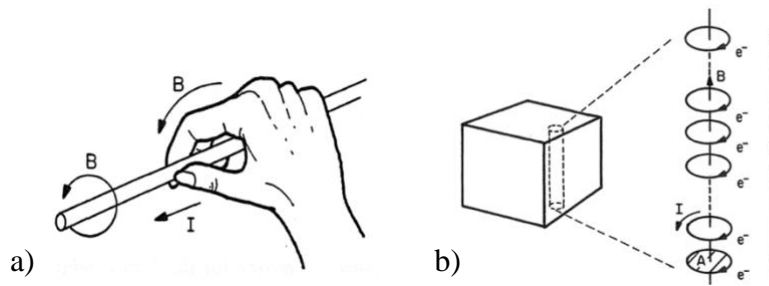
Figure 1.1 a) magnetic field formed around current carrying wire and b) magnetic moments formed by the orbital motion of electrons [2]

How the atomic moments are oriented with respect to each other over a long range is what is used to characterize ferromagnetic materials. Ferromagnetic materials are classified as having a strong net magnetization, or strong alignment of magnetic moments. Alternatively, there are materials called antiferromagnets where the direction of the magnetic moments alternates, leading to a net-zero magnetization. Figure 1.2a shows ferromagnetic atomic moment orientations which can be compared to the antiferromagnetic moment orientations in Figure 1.2b.

4
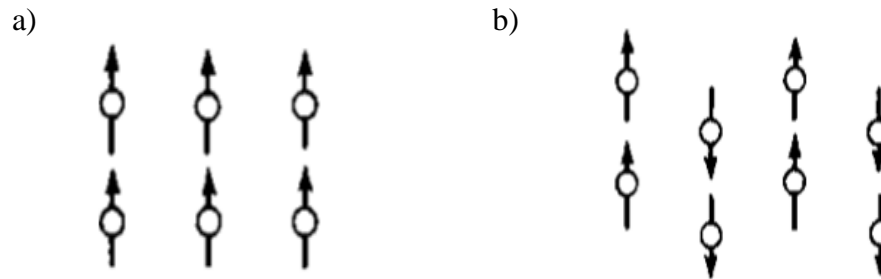
Figure 1.2 a) atomic spin alignment in ferromagnetic materials and b) spin alignment in

antiferromagnetic materials [3]

1.2.2 History of Magnetic Domains

One can make two important observations about ferromagnetic materials: they are able to reach saturation magnetization where all magnetic moments are aligned and they can also have zero net magnetization in the absence of applied field. The ability to reach saturation magnetization was explained by Pierre Weiss in 1907 by an "internal molecular field," which was really the early version of exchange coupling. Weiss postulated that magnetic moments have a field acting between them, causing them to align parallel to each other. This internal field lends itself to long range order and opposes the tendency towards disorder brought about by thermal fluctuations. Weiss then explained the ability of a sample to have zero net magnetization at zero applied fields through the existence of magnetic domains. Domains are groupings of exchange-coupled magnetic moments. Put simply, they contain groups of magnetic moments which point in the same direction. If one were to look at a macroscopic sample in zero applied field, one would most likely see many randomly-oriented domains like that shown in Figure 1.3. Because the domains have a random orientation, the summation of all magnetic moments in the sample would add to zero net moment.
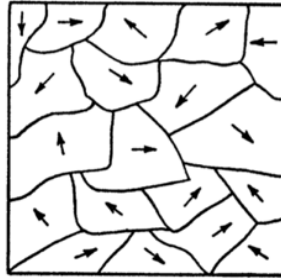
Figure 1.3 Random magnetic domain orientations in polycrystalline sample [4]

One should note that Weiss' postulations of an internal molecular force and the existence of domains were simply assumptions and were not proven to exist for another 20 or so years. Werner Heisenberg, a German theoretical physicist, proved in 1926 that Weiss' internal molecular field was really an exchange force. The existence of domains was later proven in terms of magnetic energy by Lev Landau and his student Evgeny Lifshitz. Finally, images showing the existence of magnetic domains were published in 1948 by H. J. Williams, R. M. Bozorth, and W. Shockley of Bell Telephone Laboratories [5]. The image, included as Figure 1.4, shows a photograph of domain structures for a silicon iron (FeSi) single crystal structure. The sample was prepared by electrolytically polishing the sample in a chromic acid and phosphoric acid bath. The patterns were then formed by placing drops of an iron oxide colloidal suspension on the sample and covering it with a glass slide. The domain walls were visible under a microscope once dark field illuminations were applied. These images are important because they prove the existence of magnetic domains and prove Weiss' postulation to be correct.

Figure 1.4 Photograph of magnetic domain structure in FeSi single crystal [5]

1.2.3 Magnetometry and Magnetization Curves

Prior to the publication of the magnetic domain images, people believed in the existence of domains due to the behavior seen in magnetization curves. An example of a magnetization curve has been included as Figure 1.5 below.
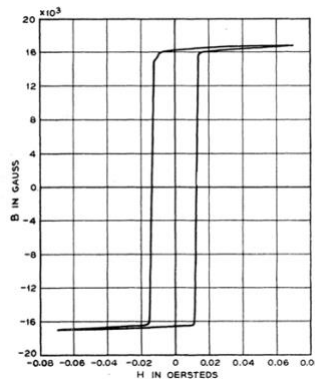
Figure 1.5 Example magnetization curve of single crystal FeSi [6]

Magnetization curves will also be called MH curves in this document as they show a sample's magnetization (M) as a function of applied magnetic field (H). These MH curves are obtained using a piece of equipment called a vibrating sample magnetometer, or VSM. A schematic and an image of VSM have been included as Figure 1.6a and Figure 1.6b, respectively. VSM works by applying a static magnetic field horizontally to a sample suspended in air by a sample holder. This

7

uniform magnetic field magnetizes the sample, which is then rapidly moved up and down. This vertical motion creates a time-alternating magnetic flux which can be sensed by the pickup coils as a magnetic moment. This measurement is taken for a wide range of applied fields and creates a dataset which reports the magnetic moment of the sample at each external applied field. When this dataset is plotted, the user can obtain their sample's magnetization curve.
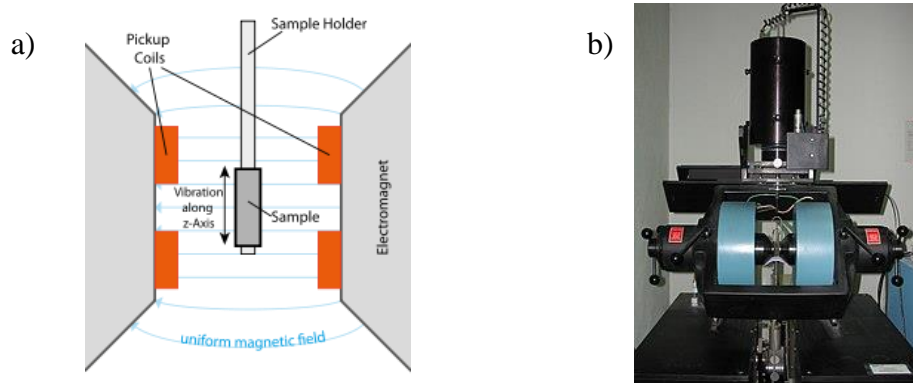
Figure 1.6 a) Schematic of vibrating sample magnetometer (VSM) and b) image of VSM [7]

VSMs generally have a somewhat low sensitivity measuring in the micro-emu range, making it difficult to measure magnetic moments of thin-film magnetic materials. There exists a more-sensitive sibling of the VSM called a superconducting quantum interference device (SQUID) VSM which can measure in the nano-emu range. Rather than using a set of pickup coils like the traditional VSM, a SQUID VSM uses superconducting loops to detect magnetic fields. The disadvantage of SQUID VSMs, however, are that they easily saturated and cannot measure large magnetic samples.

Not only are magnetization curves easy to obtain using VSM, but they also contain several important pieces of information about your magnetic samples, making them a vital test for those

working in the magnetics field. There are two magnetic characteristics that are particularly important. The first is remanent magnetization, which is representative of the magnetic moment in a sample without an applied field and is the represented by the point where the magnetization curve crosses the y-axis. The other important piece of information which can be gathered from MH curves is the susceptibility, χ, of the material. The magnetization of a sample is related to the external field by susceptibility of the sample, which is a material property and represents how easily the sample can be magnetized by an external field. This relationship is shown as Equation 1.5. Those in the magnetics community also talk about permeability which, like susceptibility, relates a sample's behavior to an applied field. Relative permeability can be related to susceptibility via Equation 1.6. An important distinction between susceptibility and permeability, though, is that susceptibility relates magnetic moment to external field while relative permeability relates magnetic flux density, B, to both external magnetic field and sample magnetic moment as seen in Equation 1.7.

$$M = \chi H \tag{1.5}$$

$$\mu_r = 1 + \chi \tag{1.6}$$

$$B = \mu_0(H + M) = \mu_0(H + \chi H) = \mu_0 \mu_r H \tag{1.7}$$

While susceptibility and relative permeability are different characteristics, they are oftentimes used interchangeably. This document will focus on relative permeability as it is more often reported by manufacturers. Some researchers in the magnetics community will refer to a material as "hard" or "soft," which refers to the magnitude of its relative permeability or how easy it is to magnetize. Hard magnetic materials generally have a low relative permeability value and require large magnetic fields to magnetize; these materials are typically used in conjunction with permanent magnets for magnetic memory applications. Alternatively, soft magnetic materials have high

relative permeabilities, making it easy to change their magnetizations. These materials are typically used for actuation and magnetostrictive cores for high power applications.

What is happening in the sample during these magnetic characterization tests can be best explained using magnetic domains. It is more energetically favorable for the net magnetic moment of each domain to align itself in the same direction as the external magnetic field, meaning that as the external magnetic field increases in magnitude, the domains will move so that they are aligned with the external field. Domain motion happens in one of two ways: domain growth or domain rotation. Domain growth occurs when domains that are aligned with the external field grow as domains in the opposite direction shrink. This occurs at lower external fields and is depicted in Figure 1.7 which shows growth of the domain aligned with the external field up to a certain point near saturation.
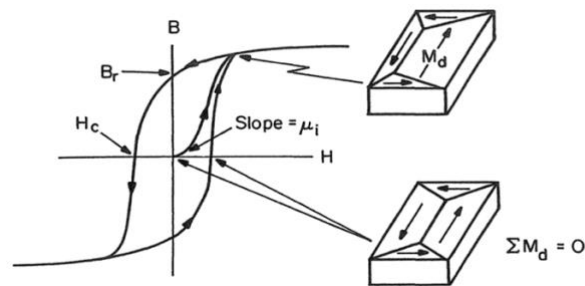
Figure 1.7 Depiction of magnetic domain growth as magnetization nears saturation [2]

Past a certain magnitude of external field, though, domains move and reorient themselves by rotating until they are aligned properly. Note that this occurs at large fields because it takes a significant amount of energy to rotate domains as opposed to growing them. The size of magnetic

domains is affected by the balance between four different types of energy: magnetocrystalline anisotropy energy, exchange energy, magnetostatic energy, and magnetoelastic energy.

1.2.4 Magnetocrystalline Anisotropy Energy

Materials with magnetocrystalline anisotropy (MCA) have preferred directions of magnetization within a crystal. These preferred magnetization directions lie along crystallographic directions; for example, a body centered cubic (BCC) iron crystal has preferred magnetization directions along its cube edges: [100], [010], and [001]. These preferred magnetization directions are often referred to as "easy axes." The converse of the easy axis is the hard axis: there exists axes in crystals which require significant energy to magnetize in that direction. The hard axis in a BCC iron crystal is the diagonal [111] [4]. As previously stated, magnetocrystalline anisotropy only applies to materials which have crystalline structure; amorphous materials, like Metglas, do not have any order so there are no easy or hard magnetization axes and MCA does not affect the magnetic domains of these amorphous materials.

MCA can be quantified as an energy density, ε_{anis}, included as Equation 1.8 [8]. This energy reflects the energy required to magnetize a sample along the hard axis.

$$\varepsilon_{anis} = -K_{u1}(\vec{u} \cdot \vec{m})^2 - K_{u2}(\vec{u} \cdot \vec{m})^4 \tag{1.8}$$

K_{u1} and K_{u2} are both anisotropy constants with units of ergs/cc and is experimentally determined. The vector $\vec{m}$ is the normalized magnetization of the sample, while $\vec{u}$ is the anisotropy vector and refers to crystallographic directions. Finally, B_{sat} refers to the saturation magnetic flux density in units of T, or the maximum flux density the material can reach.

Another way to think about these different forms of energy is in the effective field they create. This effective field can be described as the field that is "felt" by the magnetization and is important for the Landau-Lifshitz dynamic magnetic model described later. The effective field from MCA is shown below as Equation 1.9 [8].

$$\vec{H}_{anis} = \frac{2K_{u1}}{\mu_0 M_{sat}}(\vec{u}\cdot\vec{m})\vec{u} + \frac{4K_{u2}}{\mu_0 M_{sat}}(\vec{u}\cdot\vec{m})^3\vec{u} \tag{1.9}$$

1.2.5 Exchange Energy

The other type of energy which is intrinsic to a material is exchange energy. This was previously mentioned in section 2.1.2 and dates back to Weiss' 1907 internal molecular field hypothesis. The exchange force between two magnetic spins is comparable to a spring force between two objects: it represents the force pulling the spins into alignment. This push towards spin alignment encourages long range order and, therefore, larger domain size. Exchange energy's capacity for doing work can be described in terms of its energy density using Equation 1.10 [8].

$$\varepsilon_{exch} = A_{ex}(\nabla\vec{m})^2 \tag{1.10}$$

The equation for exchange energy density is similar to the spring energy equation. A_{ex} is the material's exchange constant, in units of J/m, and is comparable to the spring constant while $\nabla\vec{m}$ is the gradient of the normalized magnetization and could be compared to the displacement of a spring. Much like anisotropy energy, the effective magnetic field due to exchange energy can be written as Equation 1.11 and used in the Landau-Lifshitz equation.

$$\vec{H}_{exch} = 2\frac{A_{ex}}{\mu_0 M_{sat}}\Delta\vec{m} \tag{1.11}$$

1.2.6 Magnetostatic Energy

Interestingly, there is a type of magnetic energy which does not depend on material characteristics but depends entirely on the shape of the sample. This energy is called magnetostatic energy and often referred to as either demagnetization energy or shape anisotropy. It arises from what are called "free poles" and is a surface effect. Consider a magnetic sample with some magnetization, M, like what is shown in Figure 1.8.
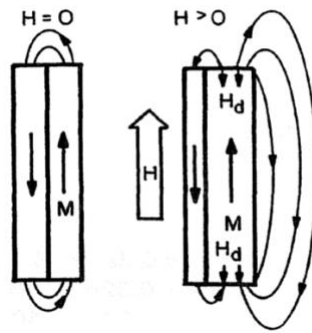
Figure 1.8 Introduction of demagnetizing field, H_d, with introduction of external field H>0 [2]

This magnet will have flux lines which must be closed loops in accordance with Gauss's law for magnetism, Equation 1.2, in Maxwell's equations. As an external field, H, is applied, the domain oriented along the external field will grow causing a larger amount of flux exiting along that alignment. We consider the magnetization M to "flow" from the south pole of the magnet to the north pole. As magnetic flux exits the north pole, however, it creates a free pole at that surface representing a south pole of a magnet. Again, this is because flux flows from south to north. This means that although the magnetization is pointing such that the top of the magnet is a north pole, there is also a pseudo-south pole at the top surface of the magnet. These free poles on the surfaces lead to an internal magnetic flux which opposed the magnetization. This internal magnetic flux or field is called the demagnetizing field and is represented mathematically in Equation 1.12:

13

$$\vec{H}_d = N\vec{M} \tag{1.12}$$

The demagnetizing field can be calculated by multiplying the magnetization, M, by a shape factor, N. This is an important point: demagnetization factor is a surface effect, so the magnitude of the demagnetizing field will increase with an increasing surface area and decreasing aspect ratio. Also note that H_d is proportional to magnetization, so it is exacerbated as magnetization increases.

The magnetic field of a sample can be written in terms of applied field, H_{ext}, and demagnetizing field, H_d, as follows:

$$\vec{H} = \vec{H}_{ext} - \vec{H}_d \tag{1.13}$$

This can be further expanded by substituting Equation 1.12 into Equation 1.13:

$$\vec{H} = \vec{H}_{ext} - N\vec{M} \tag{1.14}$$

The physical implication of shape anisotropy is that, depending on the shape of a sample, there will be directions which are easier to magnetize than others meaning that the apparent susceptibility of the sample will be different depending on the direction of magnetization. An expression for apparent susceptibility, χ_a, can be obtained by substituting Equation 1.14 into Equation 1.5:

$$\vec{M} = \frac{\chi}{1 + \chi N}\vec{H}_{ext} \tag{1.15}$$

$$\chi_a = \frac{\chi}{1 + \chi N} \tag{1.16}$$

Similarly, Equation 1.17 can be used in place of Equation 1.16 for those who prefer using permeability values [9].

$$\mu_a = \frac{\mu_r}{1 + N(\mu_r - 1)} \tag{1.17}$$

Magnetostatic energy, represented as energy density in Equation 1.18, affects domain walls in that it opposes exchange energy.

$$\varepsilon_{demag} = -\frac{1}{2}\vec{M}\cdot\vec{H}_d = -\frac{1}{2}\vec{M}\cdot\frac{\vec{B}_d}{\mu_0} \tag{1.18}$$

For exchange energy to be minimized, domain wall size must increase but for magnetostatic energy to be minimized, domain wall size must decrease. This push for smaller domain sizes is driven by the need to decrease free poles and decrease the magnitude of H_d in the domains.

1.2.7 Landau-Lifshitz Energy Model

Lev Landau and Evgeny Lifshitz published a paper in 1935 where they presented an expression for the time varying precession of a magnetic moment in a sample where there are effective fields and damping present. This equation will be referred to in this document as the Landau-Lifshitz equation and has been listed below as Equation 1.19 [8].

$$\frac{\partial\vec{m}}{\partial t} = \vec{\tau}_{LL} = \gamma_{LL}\frac{1}{1+\alpha^2}\left(\vec{m}\times\vec{H}_{eff} + \alpha\left(\vec{m}\times\left(\vec{m}\times\vec{H}_{eff}\right)\right)\right) \tag{1.19}$$

In this formulation, γ_{LL} is the gyromagnetic ratio (rad/Ts) and α is a dimensionless damping parameter. H_{eff} is the sum of MCA, exchange, and magnetostatic effective fields as well as any external fields present [8]:

$$\vec{H}_{eff} = \vec{H}_{anis} + \vec{H}_{ext} + \vec{H}_{exch} + \vec{H}_{demag} \tag{1.20}$$

The Landau-Lifshitz equation was developed for understanding thin film magnetization processes. In 1955, Thomas Gilbert updated this equation to better characterize damping. His work was motivated by the fact that while the Landau-Lifshitz equation was widely accepted and had been experimentally validated, it could not account for the large damping seen in thin Permalloy films. This was of particular interest at the time because the rate of magnetization in magnetic computer

components was severely limiting computation speed. Equation 1.21, the updated Landau-Lifshitz-Gilbert or LLG equation, incorporates an additional torque field so that the magnetic spin can orient with the applied field without increasing the rate of precession making it more accurate for highly damped systems [10].

$$\frac{\partial \vec{M}}{\partial t} = \gamma_{LL}\left(\vec{M} \times \vec{H}_{eff}\right) - \frac{\alpha}{M_s}\left(\vec{M} \times \frac{\partial \vec{M}}{\partial t}\right) \tag{1.21}$$

The difference between Landau-Lifshitz and LLG is very small for systems with Gilbert damping parameters $\alpha^2 \ll 1$. This is an attainable Gilbert damping parameter; for example, researchers have been able to develop FeGa thin films with $\alpha = 0.044$ [11]. It should also be noted that mumax, a commonly used open-source micromagnetics solver, uses the Landau-Lifshitz formulation rather than LLG. However, the difference is negligible for systems with $\alpha^2 \ll 1$.

1.3 Multiferroic Materials

In the previous section, the concept of ferroic materials was introduced. As previously stated, ferromagnetic and ferroelectric materials fall under this umbrella. There exist some materials called multiferroics where two or more ferroic materials are present. Multiferroic materials make it such that one ferroic order can be controlled by another ferroic order. For example, when ferroelectric and ferromagnetic materials are combined, electric polarization can be controlled with magnetic fields. This type of multiferroic, where there is coupling between magnetic fields and electric polarization, is called a magnetoelectric. We must note, though, that these terms are not mutually exclusive: not all multiferroics are magnetoelectric, and not all magnetoelectrics are multiferroic. The complicated relationship between these different categories if materials is detailed in Figure 1.9.
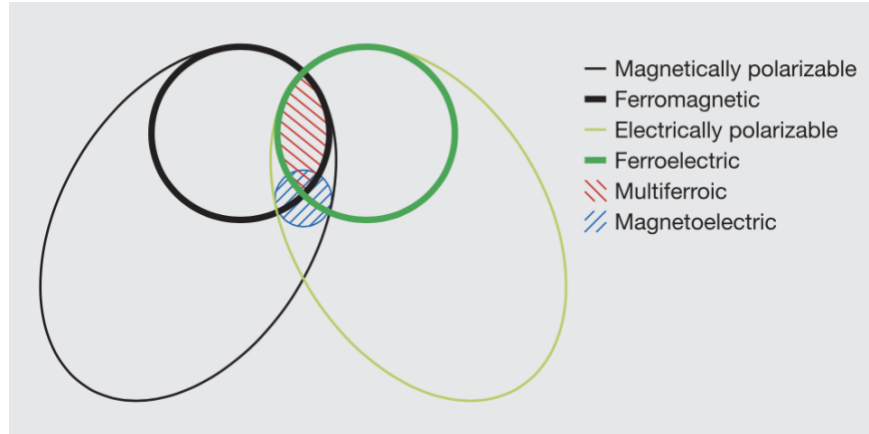
Figure 1.9 Material categories commonly used in multiferroic community [12]

Magnetoelectric materials are just one example of order parameter coupling; others include magnetostriction and electrostriction. These terms will be described in greater detail in the remainder of this section.

1.3.1 Magnetostriction

Magnetostrictive materials are those which have parameter coupling between the strain and magnetic orders. Simply put, the magnetization of a sample is coupled to the sample's strain and vice versa. This coupling is described in Equations 1.22 and 1.23 [13].

$$\varepsilon = s^H \sigma + qH \tag{1.22}$$

$$B = q^T \sigma + \mu^\sigma H \tag{1.23}$$

The mechanical behavior of the sample is described by ε, strain, σ, stress, and s^H which is the material's compliance matrix measured under constant magnetic field conditions. B represents magnetic flux density, H is the magnetic field, and μ^σ is the sample's permeability under constant

stress. Finally, q and q^T, which are equivalent in linear systems, are the magnetoelastic coupling coefficients where [13]:

$$q = \frac{\partial \varepsilon}{\partial H}\bigg|_{\sigma} \tag{1.24}$$

$$q^T = \frac{\partial B}{\partial \sigma}\bigg|_{H} \tag{1.25}$$

Put simply, q describes what output strain you could expect for a given applied magnetic field at constant stress and q^T describes what output magnetic flux density you could expect for a given applied stress at a constant magnetic field.

Magnetoelasticity affects domain wall formation just as magnetocrystalline anisotropy or shape anisotropy do, so it can also be written as an effective field and implemented into LLG. The simplified magnetoelastic effective field, H_{me}, can be written as [13]:

$$H_{me} = \frac{3\lambda_s \sigma_0 M}{2\mu_0 M_s^2} \tag{1.26}$$

M is the magnetization of the sample while M_s denotes the saturation magnetization of the material. Similarly, λ_s is the saturation magnetostriction. μ_0 is equal to the permeability of free space, $1.256 \times 10^{-6} \frac{Wb}{A \cdot m}$, and σ_0 is an applied prestress. If one were to implement LLG for a magnetostrictive material, they would incorporate Equation 1.26 into Equation 1.20, resulting in:

$$\vec{H}_{eff} = \vec{H}_{anis} + \vec{H}_{ext} + \vec{H}_{exch} + \vec{H}_{demag} + \vec{H}_{me} \tag{1.27}$$

Equation 1.27 could then be inserted into Equation 1.19 or 1.21, depending on which Landau-Lifshitz formulation is preferred, to solve for the system's magnetodynamics.

One should note that magnetoelastic systems are often referred to as magnetostrictive or piezomagnetic. These terms are often used interchangeably, but they do not mean the same thing. Magnetoelastic is a general, blanket term to specify that a material's magnetic and mechanical orders are coupled. Piezomagnetic means that there is a linear relationship between strain and applied magnetic field, while magnetostrictive means that there is a quadratic relationship between strain and applied magnetic field. This document will use magnetostrictive and magnetoelastic interchangeably for simplicity.

The first recorded observation regarding magnetostriction was by Joule in 1842 when he noticed that a bar of iron changed length when it was magnetized. Strains induced by applied magnetic fields, as described by Equation 1.24, is sometimes referred to as the Joule effect. The inverse effect, sometimes called the Villari effect, was observed by Villari in 1865 when he noticed a change in a sample's magnetization when it was stretched [14]. Starting around the 1970s, there were significant advancements in magnetostrictive technology: Terfenol-D was developed by the Naval Ordinance Lab in the 1970s for use in sonar technology [15]. It is named for the elements which it contains: terbium, iron, and dysprosium. The "-nol" stands for Naval Ordinance Lab in reference to the creators of Terfenol-D. Later in the 1990s, Galfenol was developed by the Naval Ordinance Lab [16]. Similar to Terfenol-D, Galfenol was named for the lab as well as the elements used: gallium and iron. Terfenol-D and Galfenol are frequently used in transducers, actuators, and sonar applications.

1.3.2 Piezoelectricity

Similar to magnetostriction, piezoelectricity describes coupling between strain and electricity. Piezoelectrics can be classified as multiferroics if they incorporate ferroelasticity and ferroelectricity. Note that ferroelectricity is the electric analog to ferromagnetism, meaning they experience spontaneous electric polarization. Again, this phenomenon, as with all ferroic phenomena, are brought about by the breaking of symmetry in a crystal. Also like its magnetic counterpart, piezoelectricity is often used interchangeably with electrostriction where piezoelectricity implies a linear relationship between strain and electric polarization while electrostriction implies a quadratic relationship.

Similar to magnetoelasticity, the relationship between strain and electricity in piezoelectric materials can be described using a set of constitutive equations, listed as Equations 1.28 and 1.29 [17].

$$D = \epsilon^{\sigma} E + d\sigma \tag{1.28}$$

$$\varepsilon = d^{T} E + s^{E} \sigma \tag{1.29}$$

In Equation 1.28, D is representative of electric displacement, while E is electric field. These two variables are related via ϵ^{σ}, permittivity measured at constant stress. Stress is included in Equation 1.28 as σ, which is related to electric displacement through d, the piezoelectric strain constant. Equation 1.29 describes strain, ε, as a function of the piezoelectric strain constant transpose d^{T}, electric field, stress, and the material's elastic compliance at constant electric field s^{E}. The piezoelectric strain constant and its transpose, equivalent to each other in linear systems, can be rewritten as Equations 1.30 and 1.31:

$$d = \frac{\partial D}{\partial \sigma}\Big|_E \tag{1.30}$$

$$d^T = \frac{\partial \varepsilon}{\partial E}\Big|_\sigma \tag{1.31}$$

One of the first piezoelectric materials to be investigated was Rochelle salt. Rochelle salt, or potassium sodium tartrate, was first developed by a French pharmacist around 1655 for medicinal use. It was originally called "sel polychreste" after an Ancient Greek word meaning "multiple virtues." It was not until the 1880 that it was revealed to have piezoelectric properties by the Curie brothers [18]. Rochelle salt later became a key element in electronics and acoustics following the first world war until it was surpassed in popularity by barium titanate, $BaTiO_3$, which was developed in the 1940s along with other perovskite-structured oxides [19]. Barium titanate was then replaced in 1957 by lead zirconate titanate, or PZT. PZT was preferred in part due to its higher piezoelectric coupling and its wider operating temperature range [17].

1.3.3 Magnetoelectric Technology

As previously noted, magnetoelectric materials are those which have phase order coupling between magnetism and electric polarization. These materials can exist as single-phase where the magnetic and electric phases directly couple to one another, or they can exist as indirect-coupled systems. Not all magnetoelectrics are multiferroics, but many people use these terms interchangeably. The magnetoelectric (ME) effect can exist in single-phase materials or in composite systems where the ME effect relies on strain coupling. The term "multiferroic" was first coined by Hans Schmid in 1994 in regards to ferromagnetic and ferroelectric magnetoelectric materials [20], but research concerning these materials, particularly single-phase magnetoelectrics, has been ongoing since the 1950s. In the early 1950s, the Soviet Union began combining ferroelectric and ferromagnetic

materials to form the first human-made multiferroic which they called a ferro-electromagnet [21]. The linear magnetoelectric coupling coefficient was predicted for the multiferroic compound Cr_2O_3 in 1957 and experimentally observed in the 1960s. The next big development in the field of magnetoelectric multiferroics came in the 1960s when nickel iodine boracite, $Ni_3B_7O_{13}I$, was used in the first demonstration of magnetoelectric switching [22].

The work on single-phase magnetoelectrics in the 1950s and 1960s was a huge step forward in the realm of efficient magnetization switching, but much of the work in magnetoelectrics seen now does not use single-phase, direct coupling but indirect coupling via strain. This is because single-phase magnetoelectric compounds have much lower magnetoelectric coupling coefficients, α. As explained by Nicola Spaldin and Manfred Fiebig in their 2005 publication "The Renaissance of Magnetoelectric Multiferroics," single-phase magnetoelectrics lack "large and robust polarizations" at room temperature [23]. This limitation can be expressed as Equation 1.32 [22]:

$$\alpha_{ij}^2 \leq \varepsilon_0 \mu_0 \varepsilon_{ii} \mu_{jj} \tag{1.32}$$

Here the magnetoelectric coupling coefficient, α, is written in terms of the permeability and permittivity of free space, μ_0 and ε_0 respectively, as well as the material's relative permeability and permittivity, μ and ε respectively. The limitation presented in 1.32 only applies to single-phase magnetoelectrics does not apply to magnetoelectric heterostructures. In fact, by using heterostructures instead of single-phase compounds, the coupling can be significantly enhanced by coupling the magnetic and electric phases through strain. As noted by Spaldin and Fiebig, using heterostructures allows one to have more control over the sample's magnetoelectric characteristics by optimizing the ratio, type, and microstructure of the composite's constituents. The relationship between the elastic, magnetic, and electric phases is shown in Figure 1.10 where strain, ε,

polarization, P, and magnetization, M, are controlled through stress, σ, electric fields, E, and magnetic fields, H [23].
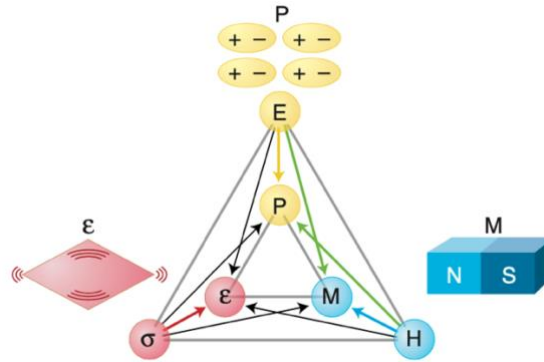
Figure 1.10 Diagram of phase order coupling in strain-mediated magnetoelectric composites

[23]

Philips Laboratory was the first group to experimentally determine that multiferroic magnetoelectric composites had large ME coupling coefficients. Experiments were conducted in the mid to late 1970s using ceramic composites of the ferroelectric $BaTiO_3$ and ferrimagnetic $CoFe_2O_4$. There was little progress in the 20 years following this discovery until the Newman Lab began researching fabrication of ceramic composites via sintering. While the fabrication process proved to be simpler than the Philips Lab's process, the coupling coefficient was much smaller. There has been a resurgence beginning in the 2000s that has seen success in creating laminates of Terfenol-D and PZT as well as composites of Terfenol-D and PVDF [24].

The magnetoelectric effect was aptly called a "product property of two-phase composites" in 1972 by van Suchtelen. This effect is represented by Equations 1.33 and 1.34 [24]:

$$ME_H \; effect = \frac{magnetic}{mechanical} \times \frac{mechanical}{electric} \tag{1.33}$$

$$ME_E \; effect = \frac{electric}{mechanical} \times \frac{mechanical}{magnetic} \tag{1.34}$$

Equation 1.33 describes how magnetic fields can be used to alter a composite's electric polarization: a magnetic field can be applied to the composite, inducing a strain in the piezomagnetic portion. Because the piezomagnetic and piezoelectric portions are bonded together, the strain is transferred from the piezomagnetic to the piezoelectric material. This strain in turn alters the electric polarization of the piezoelectric.

The constitutive equations for magnetoelectric heterostructures look much like those for magnetostrictive and piezoelectric materials. The ME constitutive equations, Equations 1.35-1.37, list stress, σ, electric displacement, D, and magnetic flux, B, as functions of the elastic, electric, and magnetic inputs:

$$\varepsilon = s\sigma + d^T E + qH \tag{1.35}$$

$$D = d\sigma + \epsilon E + \alpha H \tag{1.36}$$

$$B = q^T \sigma + \alpha^T E + \mu H \tag{1.37}$$

Recall that the elastic, electric, and magnetic inputs are strain, ε, electric field, E, and magnetic field, H, respectively. The coefficients used to relate the inputs and outputs to one another have been compiled below as Table 1.1. Note that variables with a "T" superscript like d^T, q^T, and α^T denote the transposes of their respective coefficients.

Table 1.1 Strain mediated magnetoelectric inputs, outputs, and corresponding coefficients

Inputs →

	Strain, ε	Electric field, E	Magnetic field, H
Stress, σ	Elastic compliance, s	d^T	q^T
Electric displacement, D	Piezoelectric coefficient, d	Permittivity, ϵ	Magnetoelectric coefficient, α
Magnetic flux, B	Piezomagnetic coefficient, q	α^T	Permeability, μ

Outputs ↑

The magnetoelectric coefficient can be written in terms of the piezoelectric coefficient and piezomagnetic coefficients as seen in Equation 1.38:

$$\alpha = k_c q d \tag{1.38}$$

The magnitude of the magnetoelectric coupling coefficient, α, is bound by the coupling factor, k_c, the piezomagnetic coefficient, q, and piezoelectric coefficient, d. The coupling factor is bound by the inequality: $0 \le |k_c| \le 1$ [24]. In order to achieve a large magnetoelectric coupling coefficient, which is typically favorable, these three components would generally be maximized.

1.4 Communication Devices- Conventional and Multiferroic

Constantine Balanis described an antenna's function in his *Antenna Theory: Analysis and Design* textbook when he wrote "the antenna is the transitional structure between free-space and a guiding device" [25] where the guiding device would be some form of transmission line. The first antennas and radio systems were developed by Heinrich Hertz in the mid to late 1880s, during which time he served as a professor of physics at Germany's Karlsruhe Institute of Technology [26]. He created the first complete radio system in 1886 for a set of experiments by creating what would later be called a Hertzian dipole antenna and coupling it to a single-turn loop featuring a small gap.

The Hertzian dipole he created was simply a straight wire with a spark gap at the center connected to an induction coil. This set-up, shown in Figure 1.11, was used to demonstrate tuning and resonance of antennas.
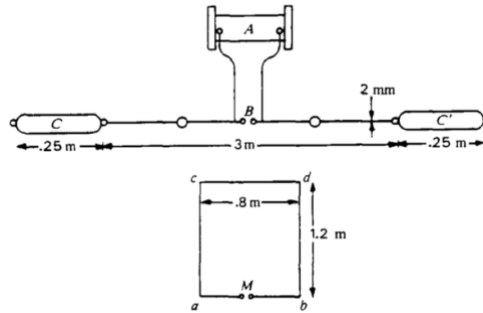
Figure 1.11 The first radio system created by Heinrich Hertz in 1886 [26]

Hertz later went on to prove Maxwell's postulation of a displacement current, $\frac{\partial D}{\partial t}$, featured in Ampere's law (Equation 1.4). Hertz also created and measured standing waves in a wire and in air, demonstrated the skin effect, and demonstrated beaming, reflection, and refraction of electromagnetic waves.

This section will contain a description of the various types of conventional antennas and their operating principles as well as in introduction to the operating principle of multiferroic antennas and discussion on the motivation for using multiferroic antennas. This section will also feature descriptions of multiferroic antenna experimental demonstrations. As noted in the previous section, the terms multiferroic and magnetoelectric are often used interchangeably, which is particularly prevalent in the antenna space. This section will use these terms interchangeably to maintain consistent with what researchers have published regarding their work. It should be noted,

however, that there exist devices which only use the piezoelectric effect making them multiferroic but not magnetoelectric.

1.4.1 Conventional Antennas

In transmitting mode communication systems, electromagnetic waves are generated by a source and guided by transmission lines and antennas until they are released into free space at the antenna-media interface. In order to understand how these systems work, we will begin by looking at the formation of electromagnetic radiation. The simplest system to look at is a single conducting wire like that shown in Figure 1.12 [25].
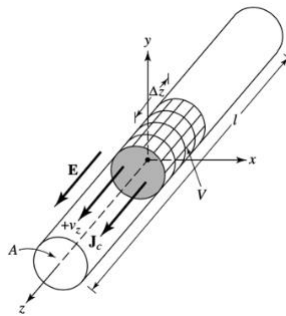
Figure 1.12 Schematic of uniformly distributed charge moving along conducting wire [25]

Conducting wires are characterized by the motion of charges and development of electric currents. Looking at Figure 1.12, there is a uniform distribution of charge which is moving along the z-direction with velocity v_z. For a thin wire whose radius approaches zero, the current within the wire can be written as:

$$I_z = q_l v_z \tag{1.39}$$

Where I_z is the current in the z-direction, q_l is the electric charge per unit length, and v_z is the velocity of the electric charges. If the current is time-varying, the derivative with respect to time of Equation 1.39 can be written as:

$$l\frac{dI}{dt} = lq_l a_z \qquad (1.40)$$

In Equation 1.40, $\frac{dI}{dt}$ is representative of the time derivative of current, l is the length of the wire, and a_z is the acceleration of electric charges in the z-direction. According to Balanis, Equation 1.40 serves as the "fundamental relation of electromagnetic radiation" [25]. This fundamental relation states that in order to have electromagnetic radiation, there must either be time-varying current or an acceleration of charge. Note that the term "acceleration" refers to a change in velocity and can be an increase or decrease in velocity over time. The implications of Equation 1.40 are that if a charge has acceleration, it will create radiation even in straight wires but that if a charge is moving at a constant speed, it must be doing so in a wire featuring some sort of curvature or discontinuity in order to create radiation.

Antennas can be separated into a handful of categories. Wire antennas are the simplest types of antennas and include dipole and loop antennas. Recall that the first antenna, created by Heinrich Hertz, was a dipole antenna. Aperture antennas include horn antennas and rectangular waveguides. Microstrip antennas, also called patch antennas, became popular in the 1970s for use in space applications and are frequently used now in commercial and government applications [25]. These antennas consist of a metallic patch on a grounded substrate. Wire, aperture, and microstrip antennas are just a handful of examples of types of antennas and can be used alone or arranged into an array to obtain favorable characteristics.

These antennas can be designed to optimize various operating parameters like radiation pattern, directivity, efficiency, and gain. However, there are some applications in which conventional antennas are inadequate due to their fundamental operating mechanisms. Implanted biomedical devices, like pacemakers, are great examples of when conventional antennas are undesirable. These types of devices require antennas that are small and can radiate through a dielectric lossy media. As antennas are scaled down and their size becomes smaller than a quarter of the electromagnetic wavelength of the signals they are set to transmit or receive, they become electrically small antennas (ESA). ESAs have fundamental limits on their performance in the form of efficiency and bandwidth. This limitation, called Chu's limit, states that as antenna size decreases, the minimum Q increases. This also translates to a lower bandwidth. The implication of this is that as Q increases and bandwidth decreases, signal distortion worsens and radiation efficiency decreases. Chu's limit, developed by Lan Jen Chu in 1948 [27], can be written as Equation 1.41 [28]:

$$Q \geq \frac{1}{k^3 a^3} + \frac{1}{ka} \tag{1.41}$$

Where k is the wavenumber, $\frac{2\pi}{\lambda}$, and a is the radius of the smallest sphere that can enclose the antenna, transmission lines, and source.

The other problem with conventional antennas previously mentioned is that they typically are not good for use in lossy media. This is because conventional antennas primarily put out electric-energy dominant radiation in the near field. Going back to the example of medical devices, the human body is considered a dielectric-cluttered environment, meaning that as electric fields pass through it, they will interact with human tissues. There are two ramifications for this: there are

29

potential safety hazards associated with high frequency electric fields interacting with human tissues and this interaction will also lead to significant attenuation of signals.

1.4.2 Multiferroic Antenna Operating Principle

Multiferroic magnetoelectric antennas offer a solution to the problems presented by antenna miniaturization and use in lossy media. Firstly, multiferroic magnetoelectric antennas can be designed to primarily output magnetic fields in the near field rather than electric fields. These magnetic fields do not interact with dielectric lossy media, meaning that they are safe to use in the human body and will not experience signal attenuation in dielectric cluttered environments.

Multiferroic antennas can also be designed to operate at low frequencies while being small in size without experiencing the limitations which electrically small antennas face because they rely on acoustic rather than electromagnetic resonance. The speed of sound is almost six orders of magnitude smaller than the speed of light, so the wavelength of an acoustic wave at a frequency would be almost six orders of magnitude smaller than the electromagnetic wavelength at the same frequency. For example, at 175 kHz, the acoustic wavelength is 1.7 cm while an electromagnetic wave at the same frequency would have a wavelength of 1.7 km. Devices should be approximately a quarter of the wavelength long to avoid ESA limitations, so magnetoelectric antennas can be as small as 0.4 cm while a conventional antenna would have to be 0.4 km to operate at 175 kHz.

Multiferroic antennas use the magnetoelectric effect and typically consist of magnetoelectric heterostructures where a piezoelectric material is coupled with a magnetostrictive material through strain. An example of a magnetoelectric heterostructure is shown in Figure 1.13a. To actuate this

antenna in transmission mode, one would input an electric signal to the piezoelectric material's electrodes, causing an electric field (E) to propagate through the thickness and induce a strain in the piezoelectric. The mechanical bond between the two phases means that the displacement at the piezoelectric-magnetostrictive interface is continuous if properly manufactured. The resulting induced strain in the magnetostrictive material would cause a magnetization change and a magnetic field (H). Finally, if properly designed, a magnetic flux would radiate from the structure. This sequence has been summed up in Figure 1.13b.
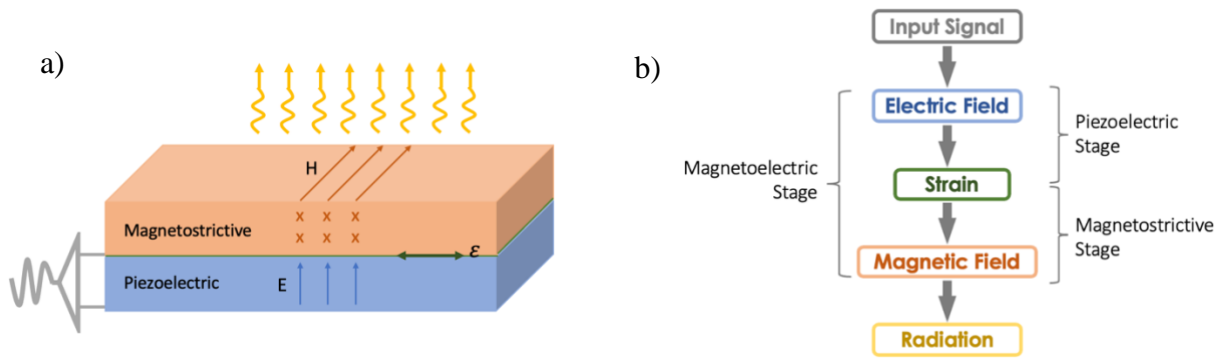
Figure 1.13 a) Schematic of magnetoelectric antenna and b) process flow for antenna operation; adapted from [29]

1.4.3 History and Development of the Multiferroic Antenna

There are three technologies which have been integral to the development of magnetoelectric antennas. They are the explosive decompression device developed in 1960, magnetostrictive transducers in the 1970s, and the magnetoelectric sensors of the early 2000s. Explosive decompression involves dramatically compressing the size of a permanent magnet over in a matter of microseconds. The permanent magnet will have an initial flux value and radius, and as the radius decreases that flux will increase due to conservation of flux. This can produce huge output

31

magnetic energy impulses, measuring up to 1,400 T [30]. These explosive decompression tests show the potential these materials have for obtaining high levels of electromagnetic radiation from magnetic materials, encouraging the development of multiferroic antennas.

Magnetostrictive transducers, similar to Figure 1.14, are used in ultrasonic transducers, sonar systems, and vibration control systems. The device shown in Figure 1.14 outputs a strain for a given electrical current input. The current is input to the solenoid, which produces an AC magnetic field. This alternating magnetic field produces an oscillating strain in the magnetostrictive (Terfenol-D) rod, which can be transmitted as an acoustic wave through a medium. In the case of sonar, this medium is sea water.
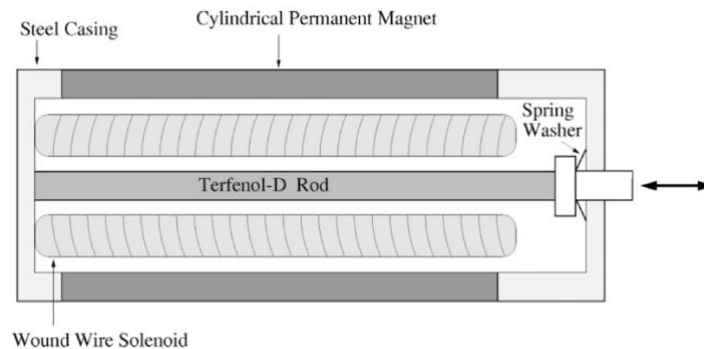
Figure 1.14 Cross section of magnetostrictive transducer [32]

Passive sonar systems were first developed in 1915 by Paul Langevin as a way to detect obstacles in the water for ships and was followed later by active sonar systems, developed during World War 1 [31]. These devices were initially piezoelectric devices, but researchers slowly began exploring magnetostrictive based sonar systems. The magnetostrictive devices have been developed and improved, but in the mid 1900s there were still discrepancies between modeling efforts and implementation of devices due to the hysteretic behavior of magnetostrictive materials.

For example, Alison Flatau of Iowa State modeled magnetostrictive transducers, like sonar, and incorporated their non-linear behavior in 2000 along with many other researchers following the discovery of Terfenol-D. While most magnetostrictive materials can behave linearly at moderate magnetic bias fields and low amplitude oscillations, the inherent non-linearity of these materials is exacerbated at high oscillating driving fields. This is due to the fact that at low bias fields, the changes in the sample's magnetization are caused by domain wall rotation, a reversible process. As the driving magnetic field is increased, magnetization changes are caused by domain movement. When the magnetic material has defects, this movement of domain walls is irreversible due to domain wall pinning. This energy loss at domain pinning sites is one contributor to the hysteresis seen in magnetization curves. While this non-linear behavior is not uncommon, it must be accounted for in models such that transducers can be designed to work in their intended environments. Flatau published two pieces of work in 2000; the first focused on the modeling of hysteresis and non-linearities in magnetostrictive transducers using energy formulations [32]. The second paper built upon the previous paper to model the dynamics of a magnetostrictive transducer as it was actuated. The result of this work was a wave equation with magnetostrictive inputs [33]. Both publications validated their proposed models against experimental data.

Magnetoelectric sensors are devices which sense the presence of external magnetic fields and output a voltage proportional to that magnetic field. They work in the reverse fashion as the transmitting mode antenna shown in Figure 1.13. In fact, magnetoelectric sensors are comparable to a receiving mode antenna. One of the early magnetoelectric sensors was developed by a group out of Virginia Technical Institute and State University in 2004. This device was a laminate in the shape of a ring, as shown in Figure 1.15, and was used to detect vortex magnetic fields from a

33

current carrying wire. It was capable of measuring fields down to the nano-Tesla range in the 0.5 Hz to 2 kHz regime. [34]
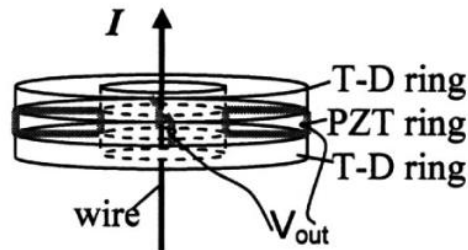
Figure 1.15 Ring-type magnetoelectric sensor for vortex fields [34]

As seen in Figure 1.15, this particular magnetoelectric sensor consisted of two Terfenol-D rings bonded to either side of a PZT piezoelectric ring. A current-carrying wire could be placed in the center of the ring and oriented along the center line. As the laminate sensed magnetic fields coming from the wire, an electric field was induced in the piezoelectric and the resulting voltage across the electrodes could be recorded. This is the same operating principle for receiving mode antennas. Multiferroic antenna theory first emerged in the early 2000's, but the first stake in the ground for the multiferroic antenna community came in 2011 when Robert Miller, William Geren, and Stephen Hubbell were awarded a U.S. Patent for a multiferroic antenna, assigned to The Boeing Company [36]. The multiferroic antenna space has since grown to include experimental validations.

1.4.4 Multiferroic Antenna Experimental Validations

Most of the experimental papers published thus far are in regards to devices that operate at frequencies in the hundreds of kilohertz regime or lower. Some work has been done in the radio frequency regime; however, it is highly difficult to make successful measurements using these

devices because they have less magnetic material and small signals, with regards to magnetoelectric antennas [37-40]. More work must be done in this frequency range to de-embed parasitic signals from the transmitted signal, which continues to be a challenge. Research in the area of multiferroic antenna modeling has been conducted, which could help predict and validate signal measurements [41,42].

One of the first published experimental demonstrations of low frequency multiferroic antennas was done by a collaboration between the Virginia Tech magnetoelectric sensor group and researchers at the Florida International University in Miami in 2019 [43]. They developed a strain-powered magnetoelectric (ME) antenna, Figure 1.16, designed to have electromechanical resonance at 30 kHz. Three devices were fabricated; one consisted of three layers of Metglas bonded to each side of a poled PZT actuator and was referred to in the paper as the poled ME laminate. One device had three layers of Metglas bonded to each side of an un-poled PZT actuator and was referred to as the unpoled ME laminate. Finally, the third device was a poled PZT actuator without Metglas, referred to in the paper as the poled PZT actuator.
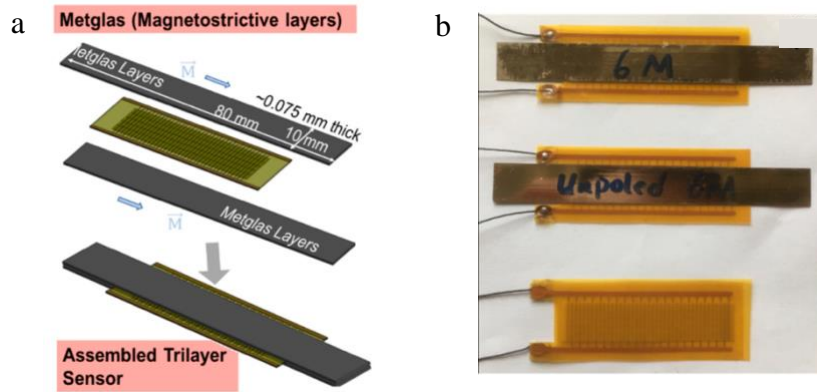
Figure 1.16 a) Schematic of trilayer antenna design and b) three fabricated devices, top to

bottom: poled ME laminate, unpoled ME laminate, and poled PZT actuator [43]

In this particular magnetoelectric heterostructure, Metglas served as the magnetostrictive portion and PZT was used for the piezoelectric portion. The unpoled ME laminate and the poled PZT actuator, the top and middle images in Figure 1.16b respectively, functioned as control samples in the experiments and were not expected to transmit any magnetic signal. Unpoled PZT will not produce mechanical strain or resonate, meaning that you would expect negligible strain from the PZT and, therefore, negligible transmitted magnetic fields. The poled PZT will resonate, but no magnetic signals will be emitted without Metglas layers bonded to the piezoelectric.

The three devices were tested one at a time using the set-up depicted in Figure 1.17. The device under test (DUT) was placed in the set-up and subjected to an external DC magnetic bias field. An electrical signal in the form of a sine wave with the same frequency as the device's resonant frequency was generated by a signal generator, enhanced by a power amplifier, and input to the antenna. Once the device was resonating, the poled ME laminate antenna output electromagnetic waves which were detected by a search coil stationed some distance away. The signal from the search coil passed through a preamplifier and could be monitored using an oscilloscope.
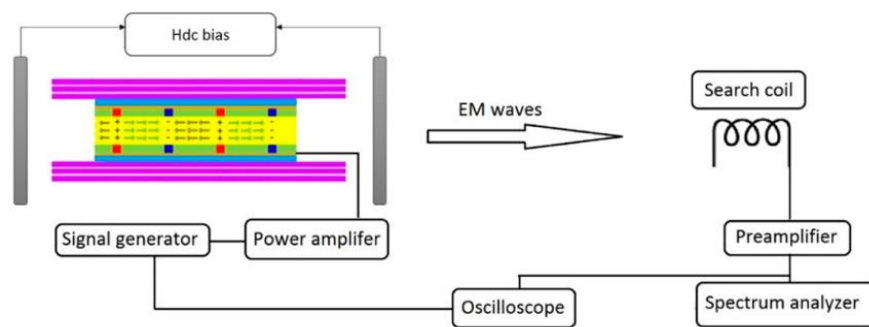
Figure 1.17 Schematic of multiferroic antenna test set-up [43]

The results shown in Figure 1.18 are a comparison of transmitted signals detected by the search coil for the three devices previously mentioned. These transmitted signals were measured as the input power to the DUT was increased. As expected, the poled ME laminate had an output signal significantly higher than the unpoled ME laminate and poled PZT laminate. The unpoled ME laminate exhibited very low transmitted signal levels. It emitted some magnetic fields because the PZT was actuating, causing current to be drawn through wires and emit magnetic fields; regardless, these magnetic fields were three orders of magnitude smaller than the fields from the poled ME laminate device. The poled PZT sample had a measured signal slightly lower than the unpoled ME laminate. It was suggested in the paper that this measured signal came from electromagnetic interference (EMI) in the room but may have also been due to the electronics and wiring used.
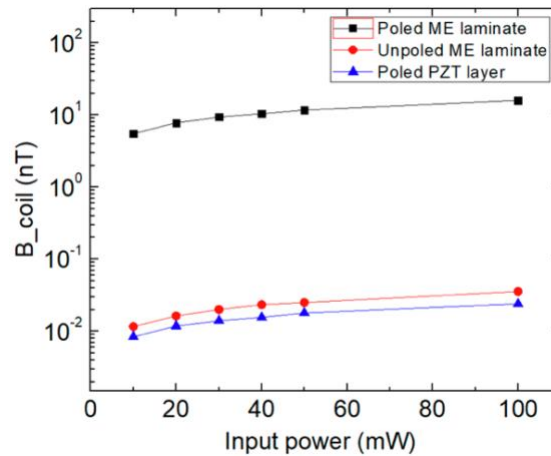
Figure 1.18 Transmitted magnetic field strength as a function of input power for three devices

[43]

Two pattern measurements were conducted on the poled ME laminate; first, the signal strength as a function of distance was measured, then the radiation pattern was measured. The signal versus

37

distance measurement was conducted for the poled ME laminate and for a loop using two different search coil placements. The search coil was placed longitudinally, $\theta = 0°$, along the sample's long axis as well as transversely, $\theta = 90°$. The transverse measurement is typically half the magnitude of the longitudinal sample. This rule is reflected in the results from this test which have been included as Figure 1.19. The search coil was first placed at a distance of 0.4 m and was then moved to 1.35 m in increments of 5 cm.
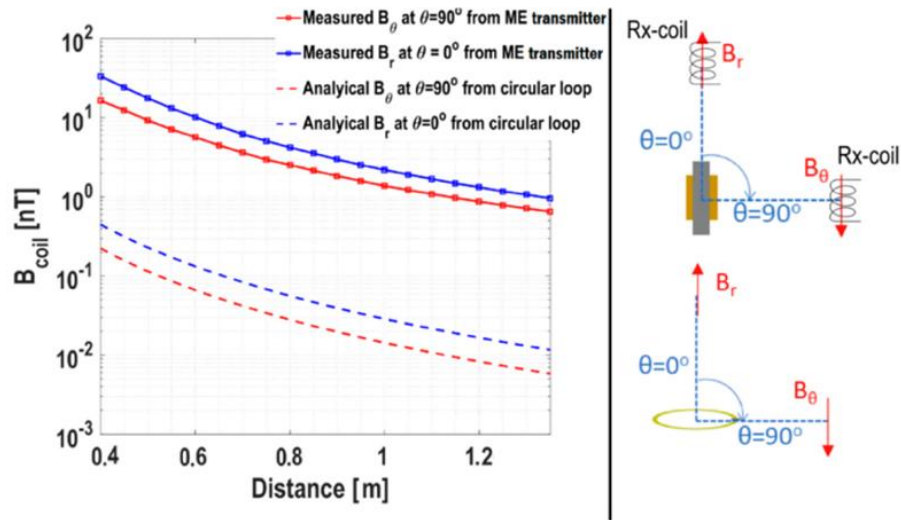
Figure 1.19 Transmitted magnetic field strength as a function of distance in the longitudinal ($\theta = 0°$) and transverse ($\theta = 90°$) directions [43]

The radiation patterns consist of a series of measurements taken at a constant distance and varying angle from the device's long axis. For example, the 0° angle corresponds to the longitudinal configuration shown Figure 1.20. Note that as the search coil was rotated about the center of the device, the probe would have been held tangent to the circle surrounding the device. The radiation patterns for the poled ME laminate are shown in Figure 1.20 and represent the normalized magnetic fields at each angle.
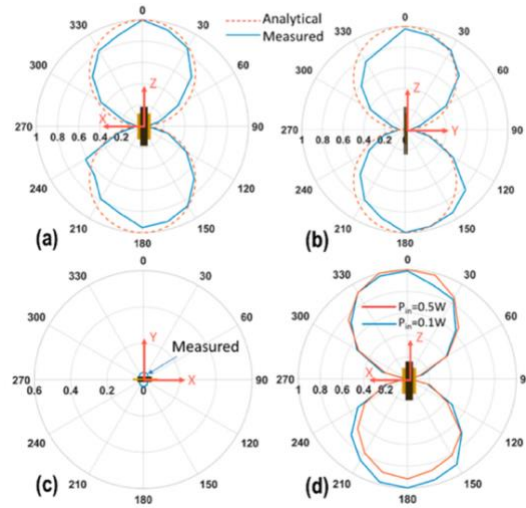
Figure 1.20 Measured radiation pattern compared to analytical predictions in the a) XZ plane,

b) YZ plane, c) XY plane, and d) comparison at different power levels [43]

This work represents one of the first publications showing an experimental demonstration of a multiferroic antenna. In the same year, though, there was second experimental demonstration paper that was published. This second device, while still a multiferroic antenna, was quite different in that it was a piezoelectric resonator which put out primarily electric fields rather than magnetic. Note that this particular transmitter would not be good for use in lossy media because of its reliance on electric energy which would attenuate in a dielectric-cluttered environment. This transmitter was created by the SLAC National Accelerator Laboratory in California and work was published later in 2019 [44]. As stated, rather than a magnetoelectric laminate, the group out of SLAC chose to use a lithium niobate (LN) piezoelectric rod as their resonator. Note that this is still a strain-mediated antenna as the LN rod had an electromechanical resonance around 35 kHz. The device's geometry is shown in Figure 1.21. The rod was approximately 10 cm long and cut into the desired cylindrical shape from a larger piece of lithium niobate. Each end of the rod had metallized

surfaces to which copper wires were soldered. The other end of each wire was connected to field-shaping toroids. There was also a modulation plate surrounding the lower toroid and connected to a capacitor and modulation switch. This modulation set-up allowed for the resonant frequency to be switched between two values 7 Hz apart.
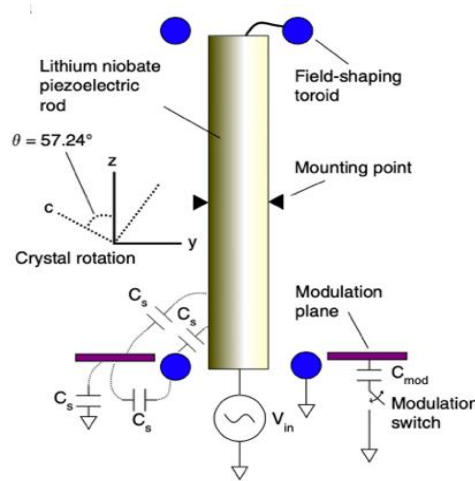
Figure 1.21 Schematic of lithium niobate transmitter, toroids, and modulation plate [44]

The LN rod was driven by a signal from a function generator. The input signal was also sent to a delay generator connected to the modulation plate. As the LN rod was resonating, two measurements were taken: the vibration characteristics of the resonator and the transmitted near field. The test set-up used to characterize those parameters is shown as Figure 1.22. A laser doppler vibrometer (LDV) was used to measure the physical displacement of the device as it was resonating. LDVs make non-contact vibration measurements of surfaces by shining a laser onto the top surface of a sample and reflecting it back. The amplitude and frequency of vibration are obtained by evaluating the Doppler shift induced by the motion of the sample's surface.

40
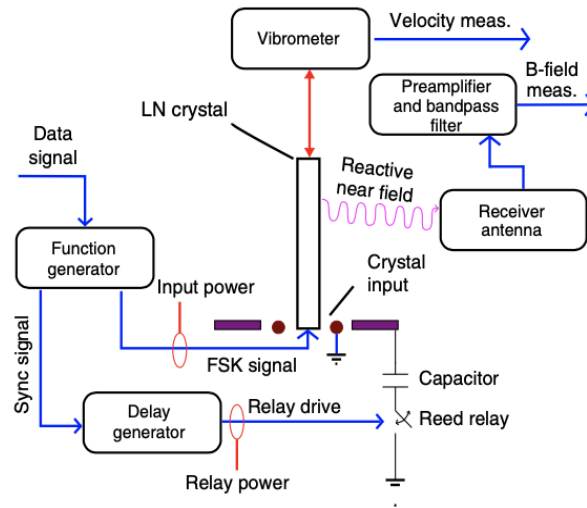
Figure 1.22 Schematic of lithium niobate rod in test set-up with driving source and measurement

equipment [44]

Prior to testing, an electromechanical model of the LN rod was created in COMSOL and was used to predict the resonator's impedance and mechanical behavior. A comparison of the experimental data and model results have been included as Figure 1.23a and b. There is good agreement between the experimental data and model results both in resonant frequency values and in magnitude of impedance and velocity.

a)
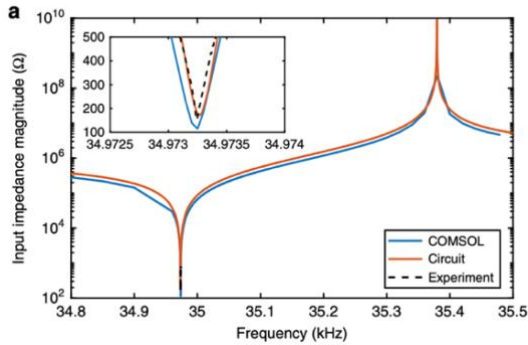
b)
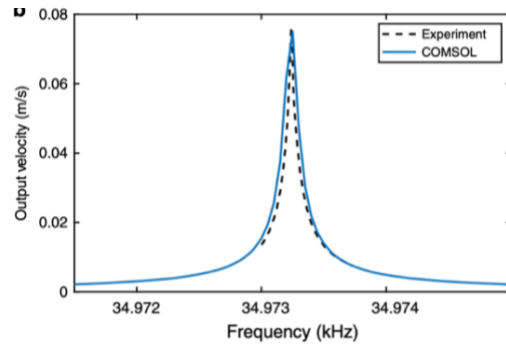
Figure 1.23 a) Impedance magnitude and b) device velocity experimental data compared to

model results [44]

As previously stated, near field measurements were conducted in addition to vibrometer tests. The electric near field was measured using a probe consisting of a 2 cm conductive sphere attached to an SMA connector while the magnetic near field was measured using a 200 turn loop. The measurements are shown below as Figure 1.24 where the red data points correspond to the measured electric field on the left y-axis and then blue data points correspond to the measured magnetic field on the right y-axis. The measurements were taken as the probe was moved away from the antenna, thus lines representing $\frac{1}{r^3}$ and $\frac{1}{r^2}$ curve fits for the electric field and magnetic field, respectively, have been superimposed over the measured data.
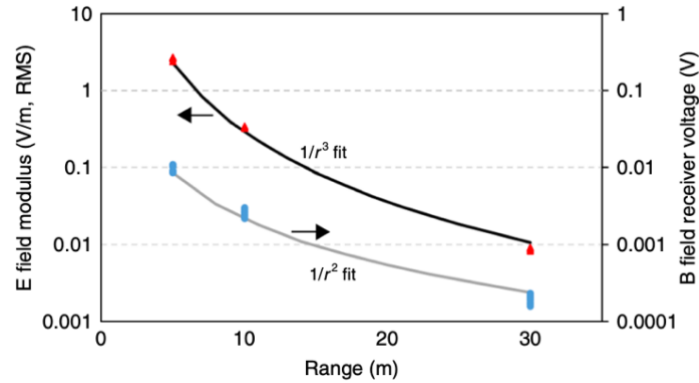
Figure 1.24 Electric and magnetic near field measurement results [44]

A third multiferroic antenna experimental demonstration paper was published in 2019 by Devin Schneider out of the Active Materials Lab at the University of California, Los Angeles. Schneider's experiments were not using an actual antenna, but rather used the constituents of a magnetoelectric antenna held in a housing as seen in Figure 1.25. Schneider put a 100mm PZT stack in series with a 100 mm magnetostrictive iron gallium (FeGa) rod and measured the flux output from the FeGa rod using a near field sensor as the PZT was actuated at 10 Hz. The housing was designed to fit within a solenoid which was used to apply a static external bias field. This external bias field was measured by a hall effect sensor held against the side of the FeGa rod. A third magnetic measurement was taken: a sense coil was wrapped tightly around the FeGa sample and was used to measure the change in magnetic flux of the rod, which could be directly related back to its magnetization. Finally, a strain gage was attached to the side of the FeGa rod and a load cell was placed between the PZT and FeGa to measure axial strain in the rod and applied stress as the PZT was actuated.
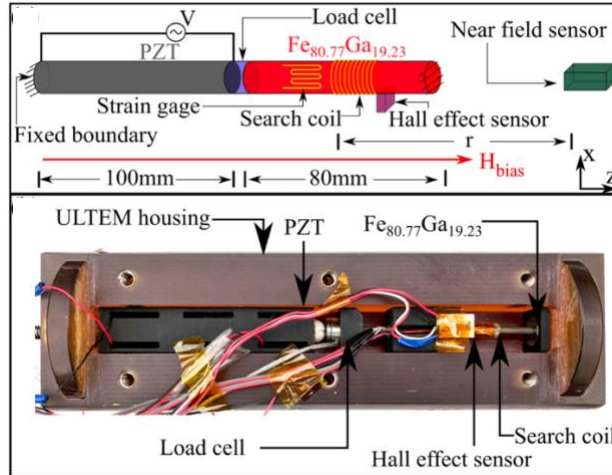
Figure 1.25 Schematic and image of test set-up including PZT actuator and FeGa rod [45]

The data from the load cell, search coil, and near field sensor are shown as a function of time in Figure 1.26a. It should be noted that the stress, FeGa rod magnetic flux, and magnetic flux in air are in phase with each other. More measurements were taken as the applied bias field was varied and as the magnitude of the electric field applied to the PZT was varied. These results are compiled in Figure 1.26b. The largest magnetic field in air, or the transmitted magnetic field, was obtained with the largest electric field as the field is directly proportional to strain according to Equation 1.29. The transmitted signal can also be observed as increasing, then decreasing with applied magnetic field. This can be explained in terms of magnetic domains; at zero bias field, one would expect a very small signal as the FeGa is subjected to an oscillating stress because the domains are in a random, disorganized orientation. However, as the bias field increases, the domains become aligned resulting in more coherent changes in the sample's magnetization. As the sample reaches saturation magnetization, though, the domains can no longer rotate and the flux out of the sample decreases and approaches zero flux output.
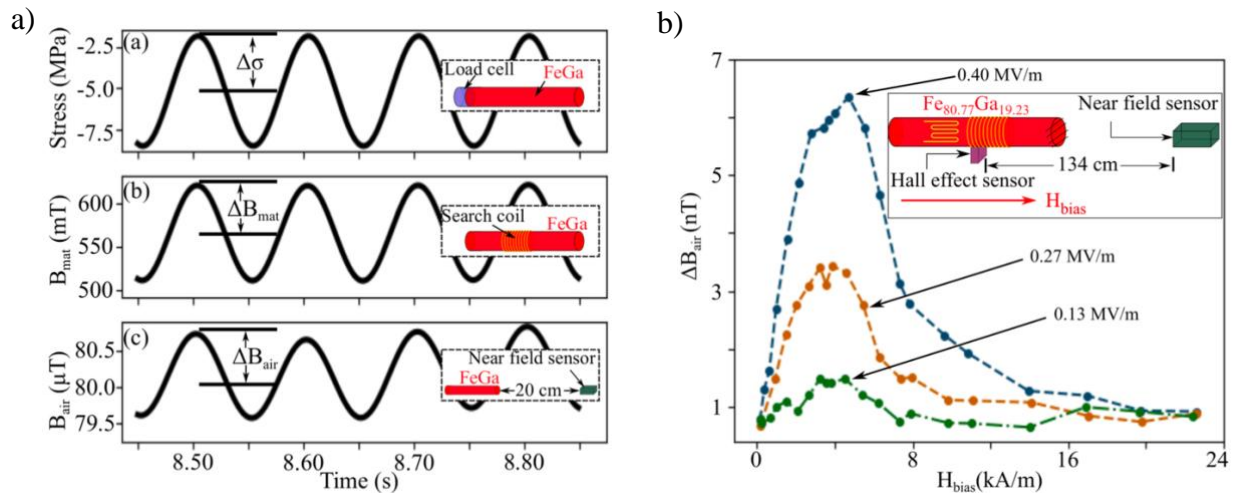
Figure 1.26 a) measured stress, flux within the sample, and flux within air as a function of time and b) flux in air as a function of external bias fields at different PZT inputs [45]

As previously mentioned, parasitic signals are a major concern when measuring transmitted signals from antennas. In order to predict transmitted signals from a multiferroic antenna, Schneider developed an analytical model which calculated the magnetic and electric fields for an infinitesimally small magnetic or electric dipole. The model is based off of Manteghi and Ibraheem's publication "On the Study of Near-Fields of Electric and Magnetic Small Antennas in Lossy Media" [46] which described loss mechanisms for small antennas in lossy media and formulated equations to predict the antennas' outputs. Schneider used his dipole model to predict transmitted magnetic fields under a variety of inputs for an antenna in air and compared the model's results to his experimental data, as seen in Figure 1.27. There was good agreement between the dipole model and experimental results confirming that the transmitted signal was coming from his FeGa rod rather than external electronics or parasitics. This dipole model is now frequently used to predict multiferroic antenna performance.
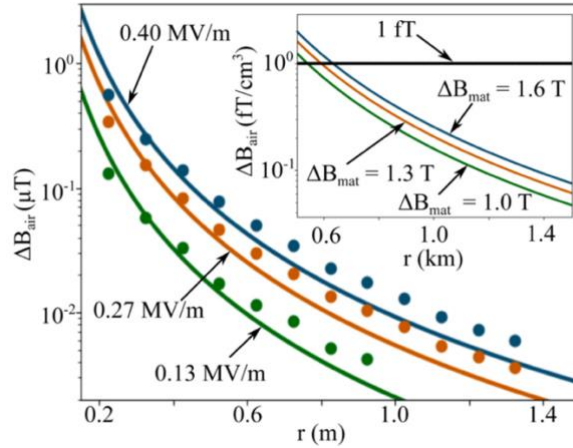
Figure 1.27 Comparison of transmitted magnetic signal experimental data to dipole model

predictions [45]

While the Virginia Tech group successfully built and tested a low frequency magnetoelectric transmitting antenna and Schneider validated experimental data with his dipole model, one of the first demonstrations of communication from a magnetoelectric antenna to a loop was carried out by scientists at the Hughes Research Laboratory (HRL) in Malibu, California, in 2020 [47]. They used a bending mode magnetoelectric antenna, biased with permanent magnets, to communicate a message to a coil. They also showed transmission of magnetic fields through metal enclosures, further proving that magnetic fields can pass through dielectric lossy media [47].

Another demonstration of communication by magnetoelectric antennas was published in 2021 [48]. This work used two length extension mode magnetoelectric antennas consisting of Terfenol-D laminates bonded to a PZT actuator. Each antenna had permanent magnets placed on top to introduce a bias field and improve performance, as shown in the image in Figure 1.28. The

antennas were both 38 mm long with a cross section 12 mm side and 8.2 mm tall. The magnets placed on top were cubes with a side length of 10 mm [48].
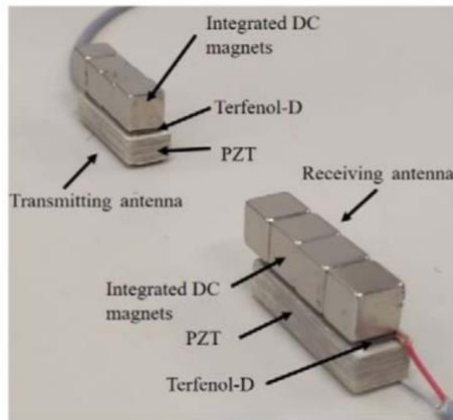
Figure 1.28 Image of transmitting and receiving magnetoelectric antennas [48]

Several measurements were taken on these devices, starting with impedance. The impedance data for one of the devices is included as Figure 1.29 and shows that the device has a series resonance at 35.8 kHz and parallel resonance at 38.65 kHz [48].
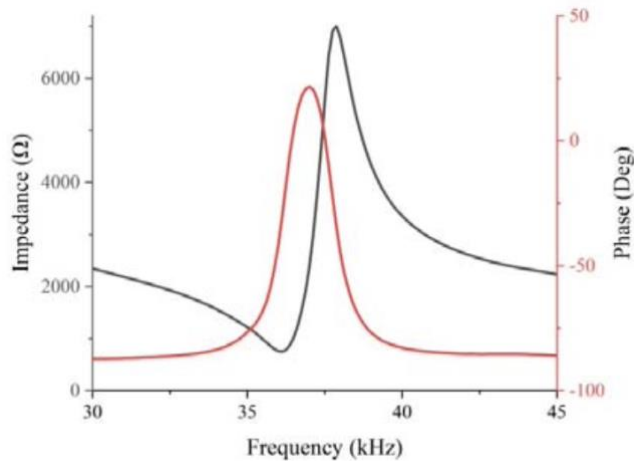
Figure 1.29 Impedance data for magnetoelectric antenna [48]

The impedance data was also used to calculate input power to the device using Equation 1.42.

47

$$P_{in} = \frac{V_{rms}^2}{|Z|} \cos \theta \qquad (1.42)$$

In this equation, V_{rms} is the input voltage to the PZT while $|Z|$ is the magnitude of the impedance

and θ is the phase angle between the current and voltage. Using Equation 1.42, the power input

was determined to be 2.03 W.

The operating frequency was also determined by measuring the voltage output of the receiving

antenna. Note that this voltage output was believed to be induced by the magnetoelectric effect in

the receiving antenna; when the transmitting antenna was actuated, it output a magnetic signal

which interacted with the magnetostrictive phase in the receiving antenna. This led to an oscillation

in the magnetostrictive portion, which was then transferred to the piezoelectric stage, leading to

an output voltage. Figure 1.30 shows the output voltage from the receiving antenna as a function

of frequency. The receiving antenna's voltage output reached a maximum at 37.95 kHz, indicating

the resonant frequency of the devices [48].
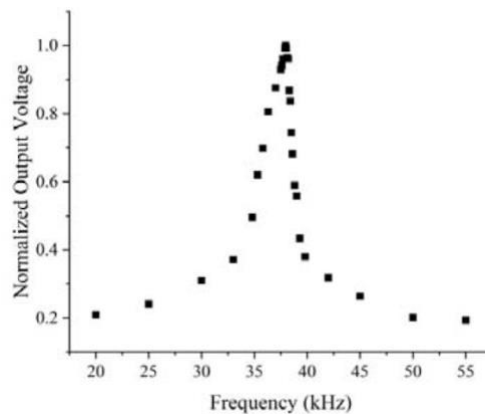
Figure 1.30 Voltage output by the receiving antenna upon receiving signal from transmitting

antenna [48]

In addition to measuring the received signal, the transmitted signal was measured as a function of bias field as well as a function of distance. The transmitted signal from the antenna with and without the bias fields as a function of distance is included as Figure 1.31. An analytical prediction of magnetic fields from a loop antenna was included in order to compare performance of magnetoelectric antennas to conventional antennas. Figure 1.31 suggests that magnetoelectric antenna signals can be an order of magnitude higher than those from conventional antennas.
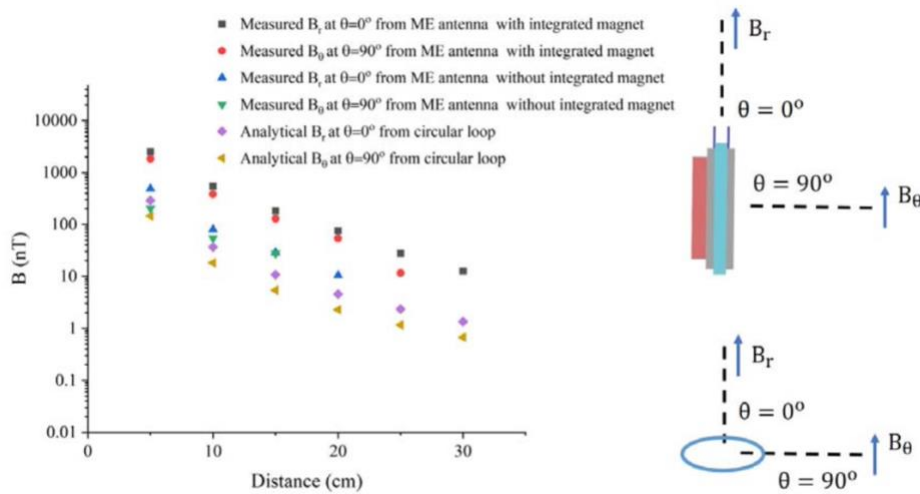
Figure 1.31 Transmitted magnetic signal as function of distance, measured for magnetoelectric device and analytically calculated for loop antenna [48]

Finally, radiation pattern measurements were taken and have been compiled as Figure 1.32. These measurements show that the behavior of the transmitting antenna corresponds to expected behavior by a magnetic dipole. These measurements suggest that the signals are primarily coming from the magnetoelectric antenna and only have small contributions from parasitic sources in the environment such as electronics or wiring.
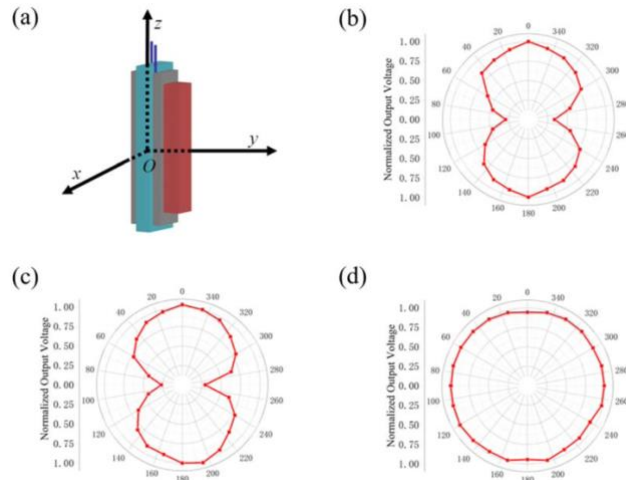
Figure 1.32 a) schematic and orientation of magnetoelectric antenna and radiation patterns for

b) xz plane, c) yx plane, and d) xy plane [48]

This work is promising in that it demonstrates the ability to transmit signals from one magnetoelectric antenna to another. These magnetoelectric antennas, in addition to the previously discussed devices, represent a promising for communicating at low frequencies with small antennas via magnetic fields.

1.5 Contributions of This Work

There have been recent advances in implantable, active medical devices which have created the desire for communication from within the body. This would be beneficial as it would allow for the transfer of a patient's data from the device implanted in the body to their healthcare provider. Now consider if implanted devices could communicate with one another- this could allow for an internet of things (IoT) and coordination of implanted devices. However, as previously mentioned, communication from within the human body presents a significant challenge. Previous attempts at communicating through the human body have relied on conventional antennas and electric fields

[49-53]. In order to minimize discomfort for patients, it is desirable to have smaller antennas. However, once conventional antennas become smaller than a quarter of the electromagnetic wavelength, their performance suffers. The human body is also a dielectric cluttered environment, meaning that electric fields are absorbed as they pass through. This is problematic from a design standpoint because signal attenuation will impact device performance, but this also poses safety concerns. As the electric component of the wave interacts with human tissues, energy is imparted to the tissues and is generally transferred in the form of heat. This is advantageous in some applications such as radio frequency ablation but is a major concern for communication devices. This interaction of electromagnetic radiation with human tissues has been reported to cause adverse reactions like localized heating and neurological issues. This can be avoided, though, by using magnetic energy dominant radiation and by operating devices at low frequencies [54], [55]. In fact, magnetic field-based devices like inductive coupling systems have been identified as safe transmission methods for implantable medical devices [56]. There have even been experiments for the Office of Naval Research which have proved that magnetic fields can propagate through lossy media, in this case seawater, with minimal attenuation [57]. In short, magnetoelectric antennas represent a promising method of communicating through the human body.

Some work has been done in the implantable transmission space, but the focus has been on using magnetoelectric devices for wireless power transfer (WPT) rather than communication [58], [59]. The focus of this work is to design, build, and test a multiferroic antenna for communication in the human body. The chosen test bed for this device is the Medtronic Micra leadless pacemaker. This device was selected as the test bed because of its size limitations, placement deep within the human body, and low frequency. The Micra is inserted into a ventricle of the heart via a catheter and is

fixed in place with Nitinol hooks. The Micra is relatively small, only taking up a volume of 0.8 cm^3 [60]. Its size relative to the human heart as well as its placement in the ventricle can be observed in Figure 1.33.
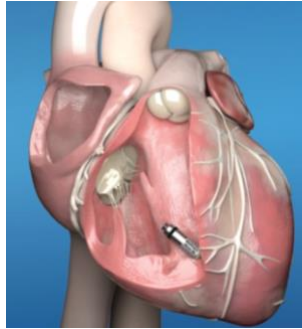
Figure 1.33 Rendering of Medtronic Micra leadless pacemaker in human heart [60]

The leadless pacemaker design is different from traditional, subcutaneous pacemakers in that the subcutaneous pacemakers sit directly under the skin and have long leads stretching down into the heart while leadless pacemakers sit directly in the heart and have electrodes on their surfaces. Communicating with subcutaneous pacemakers is simple as there is only a thin layer of skin for signals to transmit through. Communication devices for leadless pacemakers must transmit through several layers of muscle, fat, and skin, each contributing to signal attenuation.

Leadless pacemakers currently use inductively coupled loops to communicate with programmers or patient monitors [62]. Telemetry is incredibly important for pacemakers because it allows for physicians to obtain data regarding the pacing behavior of the patient's heart. Telemetry between the Micra and patient monitor occurs through coupling a current carrying loop in the pacemaker to a current carrying loop in the patient monitor, both of which have been designed to resonate at 175 kHz. Inductive coupling is commonly used technology with many benefits; however, there

are serious size limitations. Inductive coupling is a current-based system, meaning that as the loops decrease in size, their efficiency will suffer do to ohmic losses. The Translational Applications of Nanoscale Multiferroic Systems (TANMS) Engineering Research Center (ERC) funded by the NSF recommends moving away from current-based systems and conventional antennas and has been promoting strain-mediated magnetoelectric antennas as an alternative. This will allow for miniaturization without ohmic losses as they are voltage controlled. These devices also use acoustic resonance and output magnetic fields, meaning that they avoid the pitfalls associated with conventional antennas.

The multiferroic antenna proposed in this work is different than the previously mentioned multiferroic antennas in that it is a dumbbell orientation axial mode antenna. Chapter 2 focuses on characterization of this antenna, which is comprised of Metglas and PZT-5A. Chapter 3 then investigates an axial extension antenna designed to have two resonance modes to achieve high bandwidth, low bit-error-rate communication via frequency shift keying (FSK). Both chapters feature experimental work validated with Multiphysics simulations.

Chapter 2: An Axial Extension Mode Magnetoelectric Antenna

2.1 Introduction

The medical community has a need to communicate with implantable devices within the human body, i.e. a highly cluttered dielectric environment [63]. The human anatomy causes reactive near field losses as the electric components of electromagnetic (EM) waves experience significant attenuation and are unable to penetrate deep into the body, leading to serious health challenges like tissue heating [63]. Furthermore, design of electrically small antennas for the low frequency (LF) regime of 30-300 kHz required by implantable devices is extremely challenging due to the disparity between the antenna's size and the EM wavelength [27]. Recent work on multiferroic based antennas offers the potential to overcome these limitations if a better understanding can be developed of the multiferroic antenna fundamental operation, including access to a wide range of basic modeling approaches to predict the complicated electro-magneto-mechanical response.

Heterogeneous magnetoelectric antennas consist of piezoelectric actuators bonded to magnetostrictive materials, thereby enabling the coupling of electricity to magnetism through strain. During transmission, an AC voltage applied to the piezoelectric creates an oscillating strain within the magnetostrictive element, producing localized magnetic oscillations [64] which generate EM waves in the surrounding media. Magnetic materials were previously used for emitting extremely large electromagnetic pulses (EMP) by implosion in the 1960s [30] with some EM signals reaching levels large enough to damage nearby electronics. Later in the 2000s, multiferroic devices were demonstrated as highly sensitive magnetometers, with sensitivities approaching that of Superconducting Quantum Interference Devices (SQUID) in an extremely small form factor [34]. In 2009, researchers knowledgeable with both the 1960s EMP work and

the multiferroic magnetometer's high sensitivity patented the first form of a magnetoelectric transmitting antenna [36]. These relatively new magnetoelectric transmitting antennas operate at mechanical resonance with dimensions six orders of magnitude smaller than conventional antennas without using external electronics [65] but considerable work remains to be done to evaluate their response, particularly in the presence of parasitic signals from neighboring electronics and lead wires.

Schneider et al. experimentally measured the energy transfer process from a non-resonating axial multiferroic antenna (Galfenol/PZT) and verified the accuracy of a dipole model to predict the EM response in air if the material's magnetic moment is known [45]. Two 30 kHz antennas have also been experimentally demonstrated and validated with a dipole model, i.e. a longitudinal mode Metglas/PZT antenna operating at by Xu et al. [43] and a longitudinal piezoelectric/ferroelectric single crystal LiNbO resonator by Kemp et al. [10]. Mukherjee and Mallick experimentally demonstrated transmission through a phantom tissue model with a 49 kHz Metglas/PVDF antenna [66]. An unpublished Metglas/PZT bending mode antenna operating at 1 kHz demonstrated near field transmission to a pick-up coil in air as well as transmissions through a conducting enclosure [47]. Dong et al. used two longitudinal mode Metglas/PZT-5A 24 kHz antennas to transmit signals at 24 kHz via direct antenna modulation (DAM) [67]. An additional transmit and receive antenna pair operating at 38 kHz using Terfenol-D/PZT-5H was demonstrated by Niu et al. and validated with a dipole model [48] while Du et al. validated their 22 kHz antenna with a lumped element Modified Butterworth-Van Dyke (MBVD) model [68]. While these studies have provided validated experimental demonstrations of magnetoelectric antennas, most if not all of these

publications do not provide sufficient modeling approaches that one could easily predict signal strength at the design stage.

This work presents a system of decoupled models to design and validate an axial extensional mode Metglas/PZT antenna for medical applications. A Landau-Lifshitz-Gilbert (LLG) micromagnetic model fed with strain predictions from finite element electromechanical simulations provide estimates of the materials magnetic moment which are input to a dipole model for predictions of signal strength. The antenna's impedance, quality factor, mechanical resonance, and radiation patterns were measured as a function of bias magnetic field, frequency, and applied voltage. Results, as well as baseline measurements, show the presence of some parasitic signals from local electronics but these parasitic signals are well below the signal strength produced from the antenna. A computational parametric study was performed with other materials, e.g. Galfenol and Terfenol-D, to show that the signal strength can be increased by 2800x or that the antenna's physical size can be substantially decreased through appropriate design. This work validates a set of modeling tools that are useful in the design and prediction of future magnetoelectric antennas.

2.2 Modeling and Test Methods

An axial extension mode Metglas/PZT-5A magnetoelectric antenna (see Figure 2.1) was studied. The antenna was designed to radiate an 88 kHz magnetic signal and operates by applying an AC electric field to the piezoelectric, inducing both an oscillating strain and magnetization in the magnetostrictive Metglas block. The structure was designed using an eddy current model, finite element coupled electro-mechanical approach, a finite difference micromagnetic solver, and an analytical dipole model to predict radiation. The structure was fabricated, and tests were performed

56

to characterize the transmitted magnetic signals in the extreme near field as well as compare measured antenna performance with analytical and computational predictions.

Metglas 2605SA1 is a conductive material that exhibits eddy current losses during magnetization oscillations. A skin depth model, Equation 2.1, was used to find the maximum allowable Metglas layer thickness in order to limit eddy current loses to <0.5% which was D = 413 μm [69].

$$D = \sqrt{\frac{2\rho}{\pi\omega\mu_r\mu_0}} \tag{2.1}$$

where ρ is resistivity, ω is operating frequency, μ_r is the relative permeability, and μ_0 is permeability of free space (Metglas 2605SA1 material properties located in Table 2.1). A 23 μm Metglas ribbon was chosen for the composite as it was well below the calculated D = 413 μm maximum and was readily available from the commercial supplier. Figure 2.1 shows an illustration of the laminated 23 μm Metglas/polymer-based structure.

Table 2.1 Metglas/polymer composite properties

Characteristic	Nominal Value
Resistivity, ρ $(ohm \cdot m)$	1.3E-6
Estimated relative permeability, μ_r (a.u.)	1000
Metglas composite Young's modulus, E_z (GPa)	86.28
Metglas composite Young's modulus, E_x (GPa)	18.09
Metglas composite density, ρ $\left(\frac{kg}{m^3}\right)$	6356
Metglas composite poisson's ratio, v (a.u.)	0.28
Saturation magnetization, M_s $\left(\frac{kA}{m}\right)$	1300
Saturation magnetostriction, λ_s (ppm)	42

The magnetoelectric mechanical structure was designed using a finite element model, implementing Newtonian mechanics coupled with Maxwell's electrostatics (e.g. piezoelectric modeling) in COMSOL Multiphysics [41]. In this electro-mechanical model, the magnetic affects are neglected as the primary focus is on the structure's mechanical response specifically resonance frequency and corresponding mode shape, dynamic strain amplitude, and quality factor. The model consisted of 31,500 tetrahedral elements and a mesh refinement study was used to confirm solution convergence. The mechanical free-free structure was modeled with a fixed-point boundary condition imposed on the center of the PZT actuator. The material properties for the Metglas-polymer laminate were calculated using a rule of mixtures approach and are included in Table 2.1 while material properties for the PZT actuator can be found in Table 2.2:

Table 2.2 PZT-5A material properties

Characteristic	Nominal Value
PZT-5A dielectric loss, $\tan\delta$ (*a.u.*)	20E-3
Electromechanical coupling factors, $d_{ij}\left(\frac{C}{N}\right)$	$d_{33} = 4 \times 10^{-10}$ $d_{31} = -1.8 \times 10^{-10}$ $d_{15} = 5.5 \times 10^{-10}$
Compliance matrix, $s_{ijkl}\left(\frac{m^2}{N}\right)$	$s_{11} = s_{22} = 1.61 \times 10^{-11}$ $s_{12} = s_{21} = 5.63 \times 10^{-12}$ $s_{13} = s_{23} = s_{31} = s_{32} = -7.94 \times 10^{-12}$ $s_{33} = 2.07 \times 10^{-11}$ $s_{44} = s_{55} = 4.75 \times 10^{-11}$ $s_{66} = 4.43 \times 10^{-11}$
Structural damping, Q_m (*a.u*)	5.59
Terminal voltage, V (*V*)	140

The antenna's Q factor was experimentally measured and incorporated into the FEM model as a loss mechanism. For the 88 kHz axial-mode resonating structure, the final geometry selected was 10 mm axial length with a rectangular cross section of 3.4 mm by 3.5 mm as illustrated in Figure 2.1. The average axial dynamic Metglas strain ε_z^{Met} was obtained by volume averaging over the entire Metglas block.
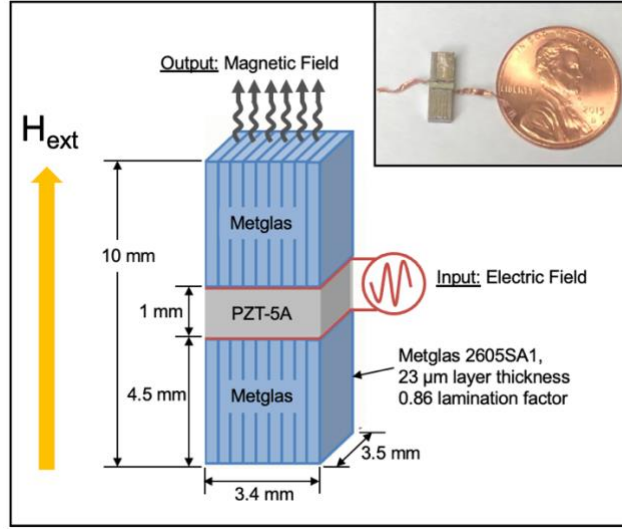
Figure 2.1 Schematic of proposed magnetoelectric antenna. Inset: Fabricated antenna with

penny for size comparison

The average strain ε_z^{Met} obtained from FEM was used to predict the magnetization change in the Metglas layers with a finite difference time domain (FDTD) approach, solving the Landau-Lifshitz-Gilbert micromagnetic system of equations [8]:

$$\frac{\partial \vec{m}}{\partial t} = \gamma_{LL} \frac{1}{1 + \alpha^2} \left(\vec{m} \times \vec{H}_{eff} + \alpha \left(\vec{m} \times \left(\vec{m} \times \vec{H}_{eff} \right) \right) \right) \tag{2.2}$$

where $\vec{m} = (m_x, m_y, m_z)$ is normalized magnetization, γ_{LL} is the gyromagnetic ratio, α is the Gilbert damping parameter, and $\vec{H}_{eff}$ is the sample's effective magnetic field. To model one of the Metglas block's geometry with micromagnetics, we assumed the primary $\vec{H}_{eff}$ terms are the external bias field $\vec{H}_{ext}$, magnetoelastics, demagnetization effects, and exchange energy:

$$\vec{H}_{eff} = \vec{H}_{ext} + \frac{9E_{met}\varepsilon_z^{Met}\lambda_s}{2\mu_0 M_{sat}^2} (\vec{u} \cdot \vec{m})\vec{u} - N\vec{M} + 2\frac{A_{ex}}{\mu_0 M_{sat}} \sum_i \frac{(\vec{m}_i - \vec{m})}{\Delta_i^2} \tag{2.3}$$

where λ_s is the Metglas sample's saturation magnetostriction, M_{sat} is the Metglas intrinsic saturation magnetization, E_{met} is the Metglas Young's modulus, $\vec{u}$ is a z-directed unit vector, N is

the shape anisotropy factor kernel for the element, A_{ex} is the exchange-stiffness coefficient, $(\vec{m}_i - \vec{m})$ is the magnetization difference between one cell and its six nearest-neighbors, and Δ_i is the cell size in the direction of neighbor i [8]. Because the size of the sample is significantly larger than what is typically modeled using LLG, it is recommended to set $A_{ex} = 0$, effectively turning exchange "off". This is considered more accurate for large geometries as the exchange length is much smaller than sample size. The model consisted of 845,000 elements and a mesh refinement study was performed to ensure convergence. The model predicts magnetic moment $\vec{m}$ changes during antenna operation for different $\vec{H}_{ext}$ and voltage-induced strains. The ferromagnetic resonance frequencies for Metglas are in the GHz regime, thus the antenna operation frequency of 88 kHz is considered quasistatic such that magnetic stable equilibrium states can be used. In addition to studying Metglas, computations were done for Terfenol-D and Galfenol with material properties listed in Table 2.3:

Table 2.3 Terfenol-D and Galfenol composite properties

Characteristic	Galfenol	Terfenol-D
Young's modulus, E_z *(GPa)*	59.43	43.28
Density, $\rho \left(\frac{kg}{m^3}\right)$	7800	9200
Poisson's ratio, υ *(a.u.)*	0.28	0.28
Saturation magnetization, $M_s \left(\frac{kA}{m}\right)$	1400	795
Saturation magnetostriction, λ_s *(ppm)*	200	1400

The resulting $\vec{m}$ from Equation 2.2 was used to predict the radiated electromagnetic (E-H) fields using a dipole model [45,46], assuming the antenna acts as an infinitesimal dipole. The spherical

dipole model consists of three equations to describe electromagnetic radiation in the three spherical directions:

$$E_\varphi = \frac{-iM\mu_r\mu_0\omega(1 + r\gamma)e^{-r\gamma}}{4\pi r^2} \tag{2.4}$$

$$B_r = \frac{\mu_0 M(1 + r\gamma)e^{-r\gamma}}{2\pi r^3} \tag{2.5}$$

$$B_\theta = \frac{\mu_0 M(1 + r\gamma + r^2\gamma^2)e^{-r\gamma}}{4\pi r^3} \tag{2.6}$$

where, i is the imaginary number, ω is operating frequency, and r is radial distance from antenna center (i.e. mechanically fixed point). M and γ, magnetic moment and propagation constant, respectively, are defined as [70]:

$$M = \frac{i\Delta z\, \Delta m_z}{\mu_r\mu_0\omega} \tag{2.7}$$

$$\gamma = \sqrt{i\omega\mu_r\mu_0(j\omega\epsilon + \sigma)} \tag{2.8}$$

Here, $\Delta z = 10$mm is the antenna length, Δm_z is the magnetic moment change considering m_x and m_y are negligible for these operating conditions, and ϵ and σ are the permittivity and conductivity of the surrounding media, i.e. air for this study.

The antenna, shown in Figure 2.1 insert, was fabricated using two laminated Metglas samples bonded to a 1mm thick PZT-5A piezoelectric solid ceramic plate obtained from commercial suppliers (i.e. Metglas, Inc. and APC International, Ltd.). The laminates consist of 152 layered 23 μm thick 2605SA1 Metglas ribbons adhered together with a polymer resin resulting in a 0.86 lamination factor (i.e. Metglas volume fraction). Prior to attaching Metglas to the PZT-5A, thin copper electrode sheets were bonded to each side of the PZT-5A sample for external electrical

leads using silver paste. Finally, the Metglas laminates were bonded to the PZT-5A using Loctite 496 instant bond adhesive and allowed to cure for 24 hours prior to testing.

The antenna was tested with a wide range of approaches to understand both the intrinsic response as well as the transmitted signal. Prior to fabrication, the magnetization versus field (MH) curve for the Metglas-polymer laminate structure was measured in a vibrating sample magnetometer (VSM) with static applied fields ranging from -375 mT to +375 mT. VSM was required as opposed to SQUID because the large magnetic moments of the sample saturated the SQUID's sensor. A ramification of using VSM, though, is that the magnitude of the applied magnetic field was limited to lower values than SQUID by the amplifier and electromagnet meaning that magnetic saturation cannot be achieved for some samples. Following fabrication, the antenna's electrical impedance was tested with an Agilent 4294A impedance analyzer acting as both a driver and sensor. A sinusoidal voltage with $V_{Max}= 0.5$ V varying from 75 to 115 kHz was input as the magnitude and phase of impedance was measured, which were used to determine the resonant and antiresonant Q factors. The voltage input to the PZT was kept minimal, i.e. $V_{Max}= 0.5$ V, in order to avoid depoling the sample during bipolar operation.

The antenna's near field radiation performance was characterized in a laboratory environment where interference-shielding expandable sleeving, ferrite cable shields, and copper-plate shields were used to limit electromagnetic interference (EMI) and parasitic signals from neighboring test equipment; however, small magnetic emissions from the lead wires were still present and are discussed along with the results. An EMI environment assessment was performed with a pseudo-antenna fabricated with aluminum blocks in place of the Metglas laminates to approximate the

magnetic "noise" floor for the test setup, i.e. no voltage-driven radiation would be produced as the magnetostrictive portion was absent. The PZT-5A was driven with 60-125 kHz AC sinusoidal voltage ranging from 0 V to a maximum of V_{Max}= 140 V generated using an HP 4195A spectrum analyzer, Agilent 33120A function generator, Trek PZD350A high voltage amplifier, and a Picosecond Pulse Lab 5530B bias tee. The spectrum analyer produced a bipolar AC voltage and the function generator produced a DC voltage. When these two were combined with the bias tee, the result was a unipolar AC voltage which was then fed into the amplifier. External magnetic biases, H_{ext}, ranging from 0 mT to 300 mT were applied using an electromagnet, except when the laser doppler vibrometer (LDV) was used due to space considerations. A Polytec OFV-552 laser doppler vibrometer (LDV) was used to measure the dynamic mechanical response at H_{ext} = 55 mT, produced with two external permanent magnets oriented axially with the sample. These tests with permanent magnets were verified with comparisons to measurements using the electromagnet.

The antenna's magnetic response was measured using a Langer LF-R 400 low frequency near-field probe. During LDV testing, the magnetic response and mechanical response were measured simultaneously. The antenna's transmitted magnetic signal was measured for the following test cases: constant distance of 3 cm with varying magnetic bias from 0 mT to 300 mT, constant bias of 180 mT with varying radial probe distance from 3 to 15 cm, and a radiation pattern under constant bias of 55 mT where the probe was moved around the perimeter of the antenna in increments of 15 degrees at a fixed distance of 3 cm.

2.3 Modeling Results and Experimental Characterization

Figure 2.2 shows the antenna's normalized mechanical displacements, $D^* = \frac{D}{D^{Max}}$ (left ordinate axis), measured and simulated versus frequency and the simultaneously measured transmitted magnetic signal, B_θ^{air} (right ordinate axis), for $H_{ext} = 55$ mT. An illustration of the test set-up and testing parameters are shown in the bottom right inset. The measured mechanical quality factor, $Q_m = 5.59$, was used as an input to the finite element model and as one can see, there is good agreement with the finite element model predictions over the entire frequency range considered. The mechanical resonance at 88 kHz is sensitive to the thickness of the bond layer between the Metglas and the PZT, which was estimated to be 0.255 mm. The low Q_m value is attributed to the relative softness of the PZT combined with the radiated energy, magnetic damping, and intrinsic polymer damping. In regards to the measured B_θ^{air} signal shown in Figure 2.2 measured at 1cm from the antenna, the trend with frequency closely follows the D^* data but does deviate at approximately 95 kHz. The magnetic signal's linear increase in this higher frequency range is attributed to magnetic emissions from the piezoelectric lead wires. The measured magnetic signal's Q factor was determined by extrapolating the leading edge of the curve at 95 kHz to the half-maximum point resulting in $Q_{mag} = 4.03$. The relatively good correlation between the displacement curves with the magnetic curves as well as the similar Q values strongly support that the transmitted magnetic signal is originating from the oscillating magnetic moments and domains in the Metglas laminate rather than parasitics from local electronics or the environment. While the measured Q values are small and limit magnetic signal strength, they do provide a larger operational bandwidth which could be useful for some applications, i.e. it's possible to trade-off of efficiency for bandwidth.

The upper right inset of Figure 2.2 shows measured impedance phase and magnitude versus frequency for the antenna with a sinusoidal voltage with V_{Max}= 0.5 V applied to the PZT. The impedance magnitude shows an electrical resonance at 88.3 kHz in close agreement with both the mechanical and magnetic signal measurements while also showing an antiresonance at 94.1 kHz. The impedance measured Q factors were calculated by evaluating the phase angle data using the phase slope method [65] with resonance $Q_r = 38$, and antiresonance $Q_a = 49$. The much smaller electric field (i.e. 2 orders magnitude smaller) used in the impedance testing excites fewer PZT domain walls, producing larger Q values compared to the antenna tests, which is also more prevalent in "soft" PZT samples such as the one used in this test. Furthermore, the smaller electric fields produce smaller Metglas strains which limit magnetic domain wall motion and produce smaller radiated fields in air and have smaller contributions from polymer damping. All of these factors yield impedance measured Q values larger than the Q factors measured in antenna tests at large electric fields in Figure 2.2. Finally, the PZT sample without Metglas attached has a larger measured $Q_m = 80$ (not shown in figure) which makes sense due to the removal of losses associated with the Metglas material. Maybe more importantly in this Metglas antenna's measured impedance curves is that $Q_a > Q_r$, suggesting that antiresonance operation may provide a more efficient mode of operation for these antennas. This comment is supported by the operation of several piezoelectric motors at antiresonance to increase the operation efficiency and conserve battery life, e.g. piezoelectric traveling wave motors [71]. Therefore, while this work does not focus on antiresonance operation, this may represent a better operational range for these antennas in the future. Specifically, the energy efficiency of this antenna could be increased by operating at the 94.1 kHz antiresonant frequency, translating into 28% higher Q (less loss) with only moderate reductions in magnetic signal strength.
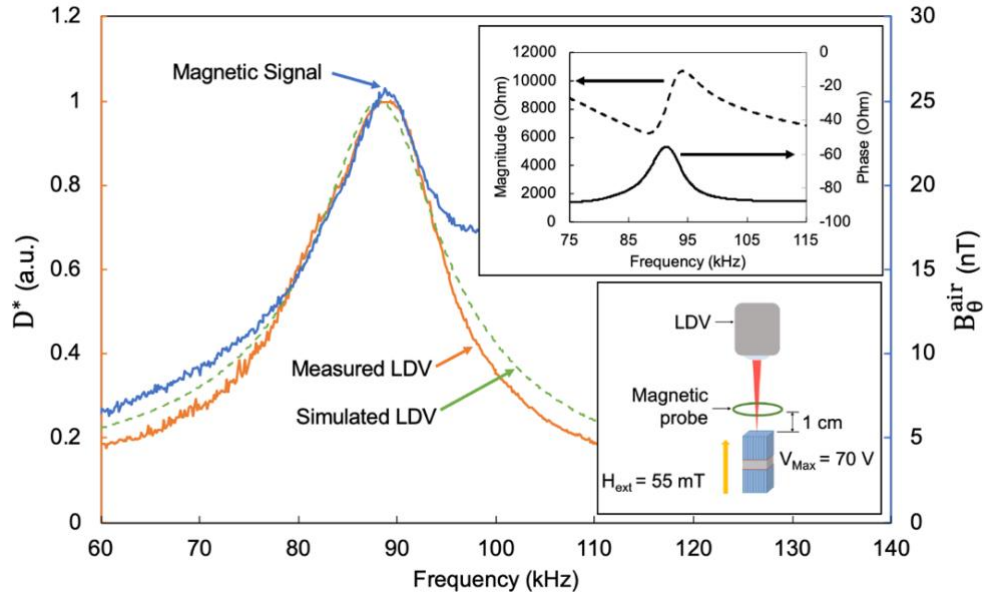
Figure 2.2 Mechanical response versus frequency overlaid with transmitted magnetic signal. Upper inset: impedance magnitude and phase versus frequency. Lower inset: Schematic of test set-up

Figure 2.3 shows VSM measured (points) and FDTD simulated (solid line) normalized axial magnetization m_z of the Metglas laminate versus applied magnetic field H_{ext}. The measured m_z linearly increases up to magnetic saturation value of $M_{s,exp} = 1.3 \times 10^6 \frac{A}{m}$. The measured relative permeability $\mu_{r,exp} = 5.9$, is reasonably close to the simulated FDTD predictions value of $\mu_{r,FDTD} = 4.4$, which is also close to the analytical prediction [9,72] for this geometry: $\mu_{r,an} = 3.09$. As can be seen in the figure, the sample magnetization saturates near $H_{ext} = 278$ mT which is also close to the FDTD simulated predictions of $H_{ext} = 300$ mT. The close agreement between simulated and measured values serve to support the predictive capability of the FDTD code even at these large dimensions. The measured and simulated permeabilities are substantially smaller

than the manufacturer's published value, $\mu_r = 52{,}000$, which is measured in a closed-loop test without demagnetization effects. The large reduction in permeability is one of the primary obstacles in generating larger signals from these antennas as magnetoelastic energy must be substantial to rotate the magnetization against the demagnetization energy.

Figure 2.3 lower right inset shows experimental (points) and FDTD predicted (solid line) Δm_z values as a function of H_{ext} bias fields for $V_{Max}= 140$ V with the antenna operating at 88.7 kHz. The experimental Δm_z values were determined from measured B_θ^{air} values (see Figure 2.4 lower right inset for setup) using the dipole model, Equations 2.6 and 2.7. At $H_{ext} = 0$ bias field in Figure 2.3 inset, one would expect Δm_z to be zero in a demagnetized sample without a bias field. However, the antenna has a saturation magnetic field applied then removed prior to testing and this, coupled with the sample's anisotropy, produces a small Δm_z at $H_{ext} = 0$. As H_{ext} increases, Δm_z increases and is attributed to increasing magnetic spin alignment producing larger magnetization changes for a given voltage-induced ε_z^{Met}. The peak $\Delta m_z = 4.09 \times 10^{-4}$ value corresponds to $B_\theta^{air} = 201$ nT at $H_{ext} = 180$ mT. As H_{ext} increases beyond this maximum, Δm_z rapidly drops, which is attributed to the sample approaching M_s as well as the increasing Zeeman energy from H_{ext}, which cannot be overcome by the oscillating ε_z^{Met} (i.e. magnetoelastic energy in Equation 2.3). Note that by using an antenna geometry with lower demagnetization energy and higher magnetoelastic energy, a substantially larger Δm_z will be produced while also reducing the required H_{ext}.

The FDTD model was also used to predict Δm_z values for the antenna shown in Figure 2.3 lower right inset. The voltage-induced average mechanical oscillations were estimated to be $\varepsilon_z^{Met} = 9$

ppm the volume (peak ε_z^{Met} = 17 ppm) as determined from the antenna's measured Q factor. The

FDTD Δm_z predicted magnitudes and trends compare favorably with the experimental Δm_z

values, however the FDTD curve is fairly coarse at lower fields (i.e. between 30 and 240 mT).

This coarseness is attributed to the relatively small amount of magnetoelastic energy (i.e. low

strains and small λ_s) in comparison to the high demagnetization energy and large sample size

which produce multiple stable energy wells at low fields. While not shown in the figure, the curve

becomes substantially smoother (i.e. similar to the experimental data) when higher magnetoelastic

energy inputs are used, i.e. higher strains and/or materials with larger λ_s. The FDTD maximum

value $\Delta m_z = 3.84 \times 10^{-4}$ at H_{ext} = 284 mT has only a 6% difference with measured Δm_z

values. However, the predicted optimal H_{ext} is 44% higher than the measured value which we

attribute to the inclusion of an exchange energy term. Exchange energy was required to minimize

local energy wells and increase stability in the low field region, however this exchange energy

increased the optimal H_{ext}. Without exchange energy present, the optimal is H_{ext} = 210 mT with

$\Delta m_z = 2.705 \times 10^{-4}$ which correlates extremely well with the experimental data. These results

indicate the FDTD micromagnetic simulations represent a reasonable approach to evaluate an

antenna sample's response to oscillating ε_z^{Met} at different H_{ext}.
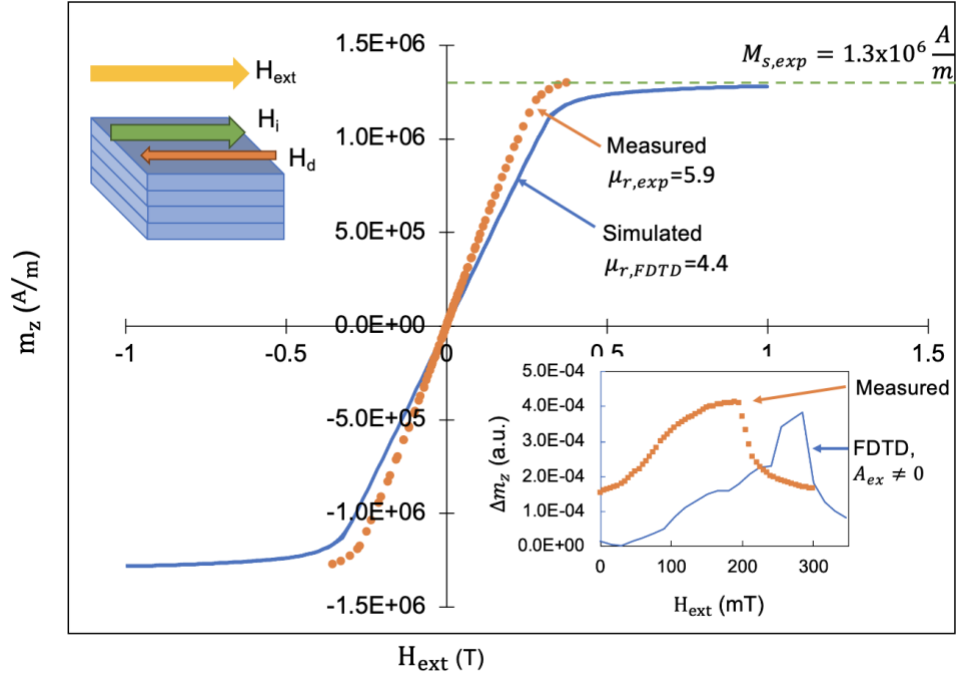
Figure 2.3 Measured magnetization versus external field data from VSM. Upper left inset:

schematic of external, internal, and demagnetization fields in sample. Lower right inset:

Measured and predicted transmitted signal versus external field

Figure 2.4 shows the antenna's B_θ^{air} measured 3 cm away from the antenna for H_{ext} values of 50

mT, 80 mT, 180 mT, and 200 mT (test setup provided as bottom right inset). Note that the curves

are representative datasets as measurements were conducted for $0 \text{ mT} \leq H_{ext} \leq 300 \text{ mT}$ increased

in increments of 5 mT. The B_θ^{air} trend with frequency in Figure 2.4 is similar to measurements

previously described in Figure 2.2: its maximum occurs at ~88 kHz and the B_θ^{air} increase above 95

kHz is attributed to surrounding cable parasitics. This parasitic signal was further confirmed with

the aluminum pseudo-antenna, resulting in a similar linear increase with frequency above 95 kHz

without a prominent B_θ^{air} peak at resonance, i.e. only ~10% larger than off-resonance.

Additionally, the aluminum antenna's B_θ^{air} was independent of H_{ext}. These results show that while

parasitics are present, the key mechanism of radiation from the Metglas antenna is Δm_z changes that were induced by an oscillating, voltage-driven ε_z^{Met}. In regards to the trends in Figure 2.4 with H_{ext}, B_θ^{air} resonance values increase from 104 nT at $H_{ext} = 50$ mT until its maximum of $B_\theta^{air} = 201$ nT at $H_{ext} = 180$ mT. For further H_{ext} increases beyond 180 mT, the value of B_θ^{air} decreases. This trend was previously described for Δm_z in Figure 2.3 bottom right inset. Additionally, the B_θ^{air} measurements below resonance at fields greater than 50 mT show an additional bending resonance mode at ~82 kHz. This additional resonance mode is predicted by the FEM model but only appears at the higher H_{ext} due to the field's influence on Young's modulus, E_{met}, which also slightly modifies the primary resonance values.

Figure 2.4 upper right inset plots the measured resonant frequency f_r as a function of H_{ext}. For $H_{ext} = 0$ mT, $f_r = 84.1$ kHz and as H_{ext} increases up 5 mT, the resonance frequency decreases to 83.6 kHz (see zoomed-in view upper right inset). The f_r decrease is attributed to the Metglas magnetic domains becoming more aligned as H_{ext} is applied. The domain alignment decreases E_{met} due to the addition of a magnetoelastic strain-softening component to the classical linear mechanical engineering strain. As the H_{ext} increases beyond 5 mT up to 180 mT, f_r monotonically increases up to a maximum of $f_r = 87.5$ kHz. The monotonic increase in f_r is due to an increase in E_{met} caused by an increase in the magnetic moments' resistance to a mechanical rotation as H_{ext} increases and approaches magnetic saturation. This initial decrease in f_r followed by an increase is referred to as the delta E effect (i.e. the increase in f_r represents an 8% increase in E_{met}) [14]. For H_{ext} larger than 180mT, there is a monotonically decreasing f_r caused by the interactions of the bending mode (see Figure 2.4 illustration) with the primary axial mode which is also suggested by the FEM model as well as reduced displacements. While this vibrational mode

interaction could be perceived as reducing the peak radiated energy, it does contribute to increasing the bandwidth of the antenna. Thus future designs may want to investigate samples with multiple bending modes near the desired operating frequency to achieve higher bandwidth.
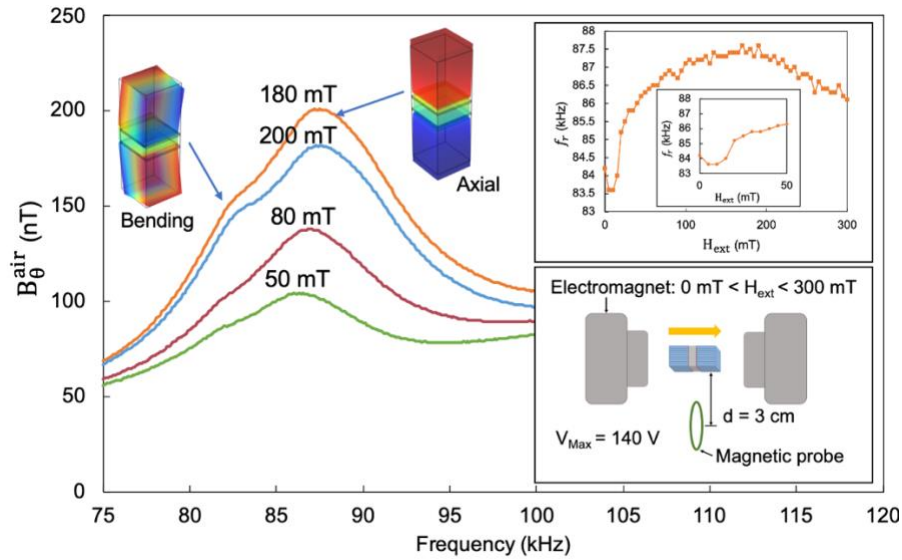
Figure 2.4 Measured transmitted magnetic fields versus frequency at three external bias fields. Upper right inset: resonant frequency of transmitted field versus external field. Lower right inset: Schematic of test set-up

Figure 2.5 shows a log linear plot of measured and dipole-predicted B_θ^{air} as a function of distance, r, from the Metglas antenna as well as dipole predictions for Terfenol-D and Galfenol antennas with larger λ_s and Q_m. All Metglas B_θ^{air} test data points ($Q_m = 5.59$) were measured with $V_{Max}=$ 140 V and $H_{ext} = 180$ mT (i.e. at the optimal H_{ext} for maximum B_θ^{air} output) while dipole model predictions were estimated with $\Delta m_z = 2.705 \times 10^{-4}$ obtained from the FDTD micromagnetic model. The experimental data ranges from a high of $B_\theta^{air} = 191.4$ nT at r = 3 cm and decreases to

$B_\theta^{air} = 1.07$ nT at r = 15 cm, i.e. following a dipole model trend of $\frac{1}{r^3}$ decay. In general, there is good agreement between the dipole model and experiments, with errors due to the considerable sensitivity to probe position during measurements. The experiments and the dipole model reach the test setup's noise floor at r = 15 cm. Note, the coil device currently used in commercial pacemakers becomes immeasurable at ~20 cm [73]. This cut-off is a desirable property for embedded medical devices as signals propagating larger distances pose personal data security issues in the form of passive eavesdroppers or active adversaries. While not shown in this figure, the dipole model has been used to validate other magnetoelectric and multiferroic antennas with favorable agreement [43-45,48]. Therefore, the dipole model is an extremely useful tool to estimate expected signals if Δm_z (or change in polarization for piezoelectric antennas) can be estimated.

Figure 2.5 inset shows measured radiation patterns for Metglas (points) and an antenna dipole prediction (solid line) with $V_{Max}= 140$ V and $H_{ext} = 55$ mT (solid line). The Langer probe's orientation at 0 degrees and 90 degrees is illustrated in the inset. There is relatively good agreement between the measured and theoretical radiation patterns in that there are two circular lobes with maximum B_θ^{air} measured at 0° and 180° and minimum B_θ^{air} at 90° and 270°. However, there are some differences in this comparison such as the asymmetry present in the left and right lobes. These differences are attributed to the sensitivity of these measurements to probe alignment as well as the large physical size of the probe, i.e. the probe measures a B_θ^{air} over a circular region of diameter 12.7 mm. Therefore, these results provide confidence that the antenna is responding as an infinitesimal dipole which is expected from the relative size of the antenna ($\Delta z = 10$mm) to the electromagnetic wavelength ($\lambda_{EM}\sim 3.4$ km) at $\omega\sim 88$ kHz.

Figure 2.5 also shows dipole simulations for a Metglas antenna with $Q_m = 1000$, computationally achieved by using a higher Q piezoelectric actuator (i.e. PZT-8 instead of PZT-5A) and by decreasing the lossy epoxy region. For $Q_m = 1000$, the strain predicted by FEM increases to 1300 ppm and Δm_z predicted by FDTD increased to 3.4×10^{-2} at $H_{ext} = 270$ mT, producing a ~190x increase in B_θ^{air} at 15 cm compared to the $Q_m = 5.59$ antenna. Figure 2.5 also shows dipole predictions for antennas fabricated with giant magnetoelastic materials, i.e. Galfenol ($\lambda_s = 200$ ppm) and Terfenol-D ($\lambda_s = 1400$ ppm) with material characteristics listed in Table 2.3. In the Galfenol predictions, the strain was 2500 ppm resulting in $\Delta m_z = 0.11$ at $H_{ext} = 345$ mT, and in the Terfenol-D predictions the strain increased to 3200 ppm strain due to the lower E_z and higher ρ and resulted in $\Delta m_z = 0.8$ at $H_{ext} = 165$ mT. As a side note, the higher field required by Galfenol is attributed to the larger demagnetization energy of this sample due to the material's higher saturation magnetization. The higher Δm_z for these antennas resulted in a B_θ^{air} increase of ~700x and ~2800x over the Metglas $Q_m = 5.59$ antenna for Galfenol and Terfenol-D, respectively, at r = 20 cm. While the reported increase in B_θ^{air} for Metglas, Galfenol, and Terfenol-D could be a concern for medical applications, the counter argument is that the volume of these antennas could be reduced by magnitudes of ~190x (Metglas $Q_m = 1000$), ~700x (Galfenol $Q_m = 1000$), and ~2800x (Terfenol-D $Q_m = 1000$) to meet the security requirements. Note that for non-medical applications where longer distance communication is desired, antennas comprised of Galfenol or Terfenol-D with $Q_m = 1000$ will have signals propagating to r = 1.13 m and r = 2.2 m, respectively (not shown in Figure 2.5).
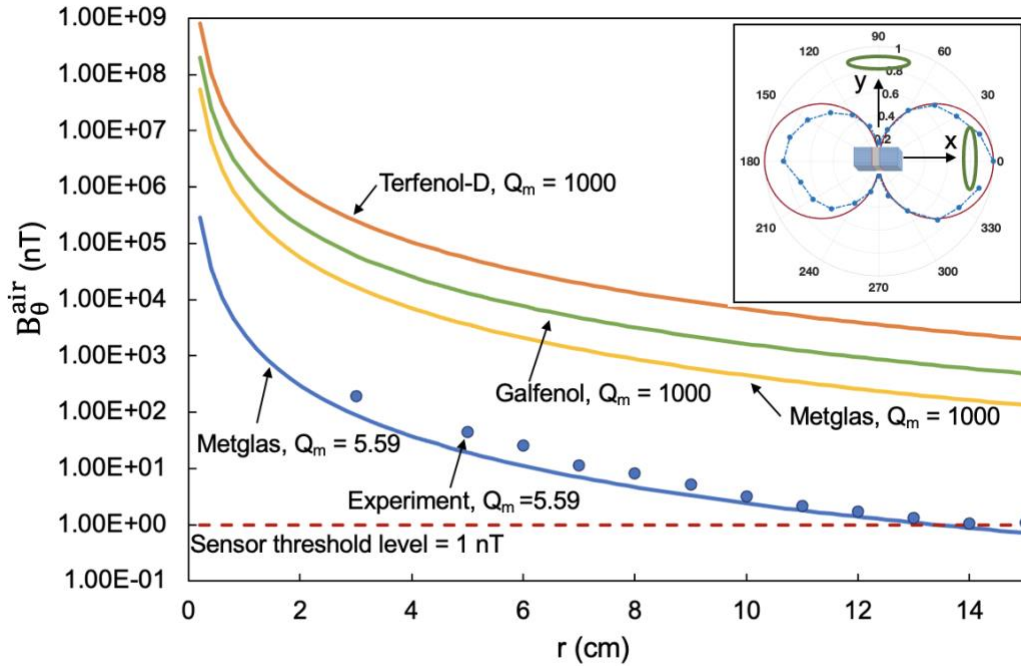
Figure 2.5 Measured and predicted transmitted magnetic signal versus distance for proposed antenna with predictions for theoretical higher-Q antennas. Upper right inset: Measured and predicted radiation pattern for proposed antenna with orientation of probe at $\theta = 0°$ and $\theta = 90°$.

2.4 Conclusion

An axial extension mode Metglas/PZT-5A magnetoelectric antenna for near field communication through lossy media was studied. The antenna consisted of two magnetostrictive Metglas-polymer composites bonded to either side of a PZT-5A actuator to form a dumbbell orientation and resonate at 88 kHz. The antenna operates by applying an AC electric field to the piezoelectric, inducing both an oscillating strain and magnetization in the magnetostrictive Metglas block, yielding EM radiation in the near field. This work presented a decoupled modelling system for predicting signal strengths in air using an analytical dipole model and a Landau-Lifshitz-Gilbert (LLG)

75

micromagnetic model fed with strain predictions from finite element electromechanical simulations. The antenna's impedance, quality factor, mechanical resonance, and radiation patterns were measured as a function of bias magnetic field, frequency, and applied voltage. The measured data had strong correlation to the simulation results, proving the efficacy of the modelling methods and validating the measured antenna response. Results show radiated signal strengths comparable to state-of-the-art pacemaker communication devices and recommendations are made for higher efficiency, higher bandwidth operation. Parametric studies were performed with other magnetostrictive materials (i.e. Galfenol and Terfenol-D) and an alternative piezoelectric actuator (i.e. PZT-8 instead of PZT-5A), determining that antennas with higher magnetostriction and Q factors could allow for device volume reduction up to 3 orders of magnitude.

Chapter 3: A Dual Band Multiferroic Antenna for FSK Communication

3.1 Introduction

The increasing demand for effective communication with implantable devices within the human body has driven the medical community to explore novel solutions to enable data transmission through highly cluttered dielectric environments [63]. However, conventional communication methods face significant challenges in such environments due to signal attenuation and energy absorption in lossy media. To address these issues, multiferroic antennas leveraging the magnetoelectric effect have emerged as promising candidates, as they predominantly emit magnetic energy in the near field, mitigating attenuation and enabling the potential for compact antenna designs. However, new approaches that focus on signal modulation for the purpose of data transmission is now warranted.

Magnetic materials were first studied as sources of EM radiation in the 1960s when it was discovered that rapid implosion of permanent magnets created extremely high levels of EM radiation [30] and this, combined with knowledge gained by the development of senstitive magnetoelectric magnetic sensors in the 2000s [34], led to the patent of a magnetoelectric transmitting antenna in 2009 [36]. In the following years, Schneider et al. experimentally measured the energy transfer process from a non-resonating axial mode multiferroic antenna (Galfenol/PZT) [45]. A longitudinal mode Metglas/PZT antenna operating at 30 kHz was developed and tested by Xu et al. showing measured signal strengths and radiation patterns [43]. Mukherjee and Mallick experimentally demonstrated transmission through a phantom tissue model with a 49 kHz Metglas/PVDF antenna, proving the capability of magnetoelectric antennas in lossy media [66].

Later, 38 kHz longitudinal mode magnetoelectric receive antenna comprised of Terfenol-D and PZT-5H was used to measure the transmitted magnetic field as a function of distance from an identical magnetoelectric antenna operating in transmit mode by Niu et al. [48].

Recent work in the multiferroic antenna space has moved on from characterizing antennas and their radiation patterns to signal modulation for the purpose of data transmission. Dong et al. used two longitudinal mode Metglas/PZT-5A antennas to transmit data at 24 kHz via direct antenna modulation (DAM) in the form of amplitude shift keying (ASK) [67]. ASK was also utilized by Du et al. in demonstrating data transmission for their 22 kHz magnetoelectric antenna pair [68]. Alternatively, some researchers have used frequency shift keying (FSK) to modulate their signals including Kemp et al. who shifted their resonance frequency by modulating the stray capacitance of the driving system for their 30 kHz longitudinal mode piezoelectric/ferroelectric single crystal LiNbO resonator [44]. An unpublished Metglas/PZT bending mode antenna operating at 1 kHz demonstrated near field transmission to a pick-up coil in air using FSK, relying on an additional piezoelectric actuator to mechanically produce frequency modulation [47]. While these studies demonstrate the ability to communicate with ASK and FSK, more work needs to be done to enable higher bandwidth and low bit error rate (BER) digital communication schemes.

This work presents the design and evaluation of a dual band antenna (i.e. magnetic radiation produced at two resonance frequencies) for higher bandwidth FSK communication. A digital communication method was chosen due to its improved performance in noisy environments and lower power requirements as compared to analog communication. Additionally, digital communication schemes are more suitable for encrypted data transmission [74], which is highly

desirable for medical applications where patient security and privacy is paramount. Frequency shift keying (FSK) was selected over other data transmission schemes because its probability of bit error is lower than amplitude shift keying (ASK) and because it has a lower level of system and processing complexity as compared to quadrature phase shift keying (QPSK) or quadrature amplitude modulation (QAM) [74].

3.2 Characterization and Communication Methods

In this study, we investigate a dual band Galfenol/PZT-8 magnetoelectric antenna designed to emit a magnetic signal at both its 83 kHz bending mode (low-frequency carrier wave) and 117 kHz axial mode (high-frequency carrier wave). Data transmission is achieved by frequency shift keying (FSK) modulation during operation. The antenna operates by applying an AC electric field to the PZT-8's electrodes, inducing oscillating strains and magnetizations in the magnetostrictive Galfenol. The antenna dimensions were selected using a system of decoupled models: i.e. finite element coupled electro-mechanical analysis, a finite difference time domain (FDTD) micromagnetic simulation, an analytical dipole model, and an eddy current simulation. Experiments initially characterized the transmitted magnetic signals in the extreme near field, followed by a demonstration of the antenna's dual band FSK data transmission.

A finite element model, combining solid mechanics and electrostatics in COMSOL Multiphysics [41] while neglecting magnetic effects, was used to select the antenna's geometric dimensions. The model used 95,662 tetrahedral elements and a mesh refinement study confirmed solution convergence. The mechanical structure was modeled with a fixed-point boundary condition imposed on the center of the PZT-8 actuator to represent experiments and the Galfenol composites

were shifted off-center of the PZT-8 to introduce asymmetry and replicate the fabricated device. A Galfenol-polymer laminate was used to reduce eddy current loss (i.e. <5%) as calculated using a skin depth equation, resulting in a layer thickness of 500 mm [69]. Material properties for the Galfenol Laminate and PZT-8 materials are included in Table 3.1. The average axial dynamic Galfenol strain ε_z^{Galf} was calculated from finite elements by volume averaging over the entire Galfenol block. The antenna's Q factor was experimentally measured and incorporated into the FEM model as a loss mechanism.

Table 3.1 Galfenol/polymer composite properties

Characteristic	Nominal Value
Resistivity, ρ ($ohm \cdot m$)	8.5E-7
Estimated relative permeability, μ_r (a.u.)	5
Galfenol composite Young's modulus, E_z (GPa)	59.43
Galfenol composite Young's modulus, E_x (GPa)	50.42
Galfenol composite density, ρ $\left(\frac{kg}{m^3}\right)$	7800
Galfenol composite poisson's ratio, v (a.u.)	0.28
Saturation magnetization, M_s $\left(\frac{kA}{m}\right)$	1400
Saturation magnetostriction, λ_s (ppm)	200

The average strain ε_z^{Galf} was used to predict the magnetization $\vec{m}$ changes for different applied external magnetic fields $\vec{H}_{ext}$ and applied oscillating voltages with a finite difference time domain (FDTD) approach [75]. The approach uses the Landau-Lifshitz-Gilbert micromagnetic solver mumax[3] [8] incorporating Zeeman energy, demagnetization energy, and magnetoelastic energy while assuming exchange energy is negligible at the dimensions modeled (i.e. millimeters). The

model consisted of 11,250 elements and a convergence study was performed to ensure convergence. The resulting $\vec{m}$ predicted from the FDTD code was fed into a dipole model to to predict the radiated electromagnetic (E-H) fields [75], assuming the antenna acts as an infinitesimal dipole.

The 10 mm long antenna consists of two 4 mm diameter Galfenol laminated composits, each 2.5mm long and attached on either side of a 5 mm square PZT-8 as shown in Figure 3.1. The Galfenol slices in the laminate were cut from a solid Galfenol sample ($Fe_{81.5}Ga_{18.5}$ from TdVib) using Wire EDM. The eight 500 mm thick Galfenol layers were adhered together with a 7 μm double sided epoxy sheet, resulting in a 0.99 Galfenol volume fraction laminate. Thin copper sheets were adhered to the PZT-8 electrodes using silver epoxy, extending past the edges of the PZT-8, for external leads. The Galfenol composites were then bonded to the PZT-8 offset 0.1 mm from the PZT-8's center using Loctite 496 adhesive and cured for 24 hours prior to testing.
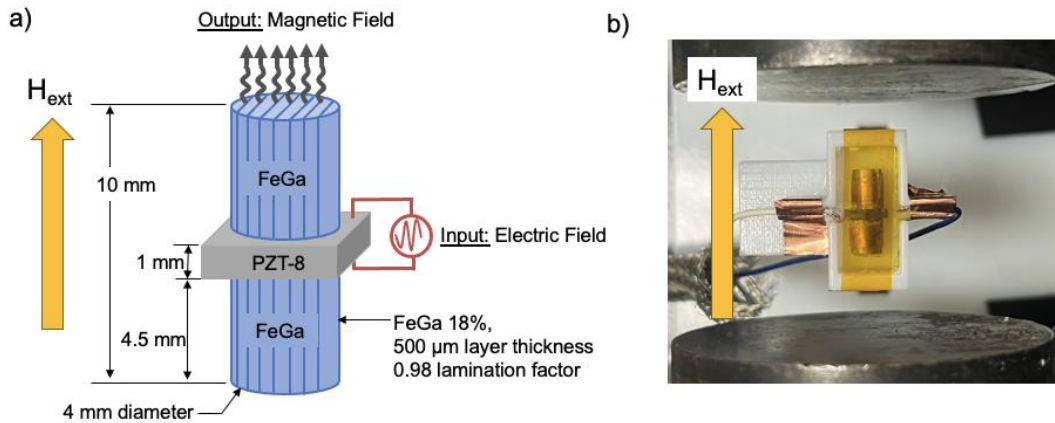

Figure 3.1 a) Schematic of dual band antenna; b) fabricated dual band antenna in electromagnet.

The Galfenol laminates M vs. H cures were measured in a vibrating sample magnetometer (VSM) with static applied fields ranging from -375 mT to +375 mT. The antenna's electrical impedance was tested with an Agilent 4294A impedance analyzer acting as both a driver and sensor with the input signal set to V_{Max}= 0.5 V AC signal varying from 50 to 150 kHz. The antenna's near field transmitted magnetic signal was characterized with a AC sinusoidal voltage input signal ranging from 0 V to a maximum of V_{Max}= 140 V generated using an HP 4195A spectrum analyzer, Agilent 33120A function generator, Trek PZD350A high voltage amplifier, and a Picosecond Pulse Lab 5530B bias tee. Static external magnetic biases, H_{ext}, were applied using an electromagnet. A Polytec OFV-552 laser doppler vibrometer (LDV) was used to measure the dynamic mechanical response with zero applied magnetic bias field. The device's transmitted magnetic signal was measured using a Langer LF-R 400 magnetic probe for the following test cases: constant distance of 3 cm with varying magnetic bias from 0 mT to 300 mT, 130 mT bias with radial probe distance varying from 3 to 10 cm, and a radiation pattern under zero bias in 30 degree increments at 3 cm.

During FSK testing, a National Instruments NI 9402 I/O DAQ device was used to record data, an HP Infinium oscilloscope was used to capture the low- and high-frequency waveforms, and the function generator was programmed to shift between the low-frequency carrier signal (83 kHz; designated as a logical 0) and the high-frequency carrier signal (117 kHz; designated as a logical 1) at a rate of 10 Hz in a set sequence forming a "hello" message in binary. Three second bursts of an 83 kHz V_{Max}= 1 V sine wave were used to add a break between letters to simplify the manual decoding of the modulated signal. The voltage input to the PZT-8 and antenna's transmitted signal were simultaneously recorded over the duration of the bitstream in order to demonstrate data transmission via FSK of a dual band multiferroic antenna.

3.3 Experimental Characterization and Communication Demonstration

Figure 3.2a left ordinate axis shows measured normalized mechanical displacement, $D^* = \frac{D}{D^{Max}}$, versus frequency while the measured transmitted magnetic signal, B_θ^{air}, measured 1 cm from the device is shown on the right ordinate axis for zero applied bias field. There are two measured mechanical resonance modes in the studied frequency range (i.e. 50-150 kHz): one occurs at 83 kHz and the other occurs at 117 kHz. The 83 kHz resonance peak has a quality factor of $Q_m = 2.9$, which was used as an input to the finite element model as a conservative estimate compared to the 117 kHz mode's $Q_m = 3.87$ quality factor. The low quality factors are due to the lossy epoxy bond layer present in the load path of the design.

The locations and mode-shapes of the measured D^* peaks were confirmed with FEM models using an eigenvalue study. Figure 3.2b shows the mechanical resonance modes from the FEM eigenvalue studies up to 150 kHz, listed in order of frequency, and accompanied by surface plots of the modes' displacements. There are two 1st order bending modes below the predicted 126.5 kHz axial mode which occur at 74.4 kHz and 74.5 kHz. There are two 2nd order bending modes above the axial mode at 136.4 kHz and 137.6 kHz. The measured 83 kHz measured mode corresponds to the simulated 74.5 kHz bending mode and the 117 kHz measured mode corresponds to a simulated 126.5 kHz axial mode. The errors between simulation and measurements were 10.7% for the bending mode and 7.8% for the axial mode and are attributed to the model's sensitivity to the asymmetry of the sample produced during fabrication as well as the rough geometries of the sample. While potentially an issue, this asymmetry contributes to a shift in the neutral axis of the Galfenol composite and this shift contributes to uneven strain distribution throughout its volume, enabling the production of magnetic radiation by the bending modes.

As seen in Figure 3.2a right ordinate axis, there are two measured B_θ^{air} resonance peaks at 83 kHz

and 117 kHz, corresponding to the measured D^* resonances, producing magnetic signals of 474.6

nT and 427.27 nT, respectively. The production of magnetic signals by the 83 kHz bending mode

is enabled by the antenna's asymmetry and the resulting uneven strain distributions. The measured

B_θ^{air} trend closely follows D^* with frequency but begins to deviate at approximately 130 kHz when

B_θ^{air} begins to increase linearly due to parasitics [75]. The antenna's quality factor calculated from

measured B_θ^{air} was $Q_m = 3.53$ at 83 kHz and $Q_m = 4.29$ at 117 kHz, further corresponding to the

antenna's mechanical performance.
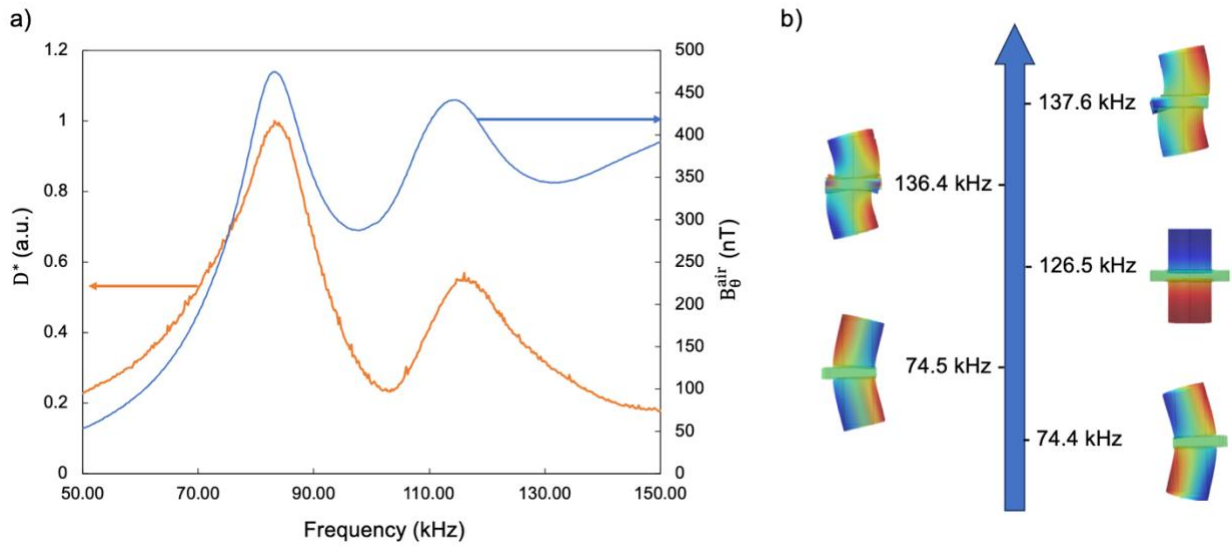
Figure 3.2 Measured mechanical displacement, D^*, and measured transmitted magnetic signal

B_θ^{air} vs frequency; b) List of modes between 0 and 150 kHz.

Figure 3.3 shows measured transmitted magnetic signal, B_θ^{air}, measured 3 cm away from the

device biased at four external magnetic fields: 15 mT, 67 mT, 159 mT, and 203 mT. The B_θ^{air}

trend with frequency in Figure 3 is similar to measurements previously described in Figure 3.2a:

its maxima occur at 83 kHz, attributed to the bending mode, and 117 kHz, attributed to the axial mode. The linear increase in B_θ^{air} above 130 kHz is present in Figure 3, but the magnitude is constant with increasing H_{ext}, supporting that these are emitted by the wire leads and are of parasitic nature. Note that these parasitic signals become negligibly small compared to the strain-mediated radiation from the antenna at higher bias fields.

Figure 3.3 inset shows the trend of B_θ^{air} with increasing H_{ext} for the 83 kHz bending mode and 117 kHz axial mode for the full set of test data, conducted for 15 mT $\leq H_{ext} \leq$ 300 mT increased over a span of 32 points. The bending mode B_θ^{air} resonance values increase from 68.9 nT at $H_{ext} =$ 15 mT until its maximum of $B_\theta^{air} =$ 268.4 nT at $H_{ext} =$ 150 mT. As H_{ext} increases beyond 150 mT, the value of B_θ^{air} decreases. Similarly, the axial mode B_θ^{air} resonance values increase from 85.46 nT at $H_{ext} =$ 15 mT until its maximum of $B_\theta^{air} =$ 293.25 nT at $H_{ext} =$ 159 mT, then decreases. The bending mode has a lower maximum signal as compared to the axial mode because the tensile side of the bending structure contributes to Δm_z while the compressive side of the bending structure results in Δm_z normal to the long axis, neither contributing to nor deducting from EM radiation. This means that half of the volume and strain of the structure contributes to radiation during bending while the entire volume contributes during axial vibration. Note that the Galfenol multiferroic antenna exhibits higher signal strengths at zero bias fields and requires a lower optimal H_{ext} as compared to Metglas multiferroic antennas [75] due to the Galfenol's higher remanence magnetization and its higher saturation magnetostriction. Additionally, the Galfenol sample was fabricated with an pre-stress, meaning lower input strains from the PZT-8 were required for substantial Δm_z to occur. The 83 kHz bending mode and 117 kHz axial mode have different B_θ^{air} vs H_{ext} trends because the composite's change in stiffness due to H_{ext} is anisotropic,

i.e. the change in E_{Galf} in the axial and in-plane direction are the same while the change in E_{Galf} through the alternating Galfenol and epoxy layers is lower.

The trends shown in Figure 3 and its inset offer insight into the optimal operating conditions for dual band multiferroic antennas, specifically that the highest signals can be achieved with a magnetic biases of approximately 150 mT. Permanent biasing at this field can be achieved by attaching permanent magnets to the top and bottom faces of the antenna (i.e. attached to the Galfenol composites), which can potentially increase the antenna's quality factor via higher inertial forces.
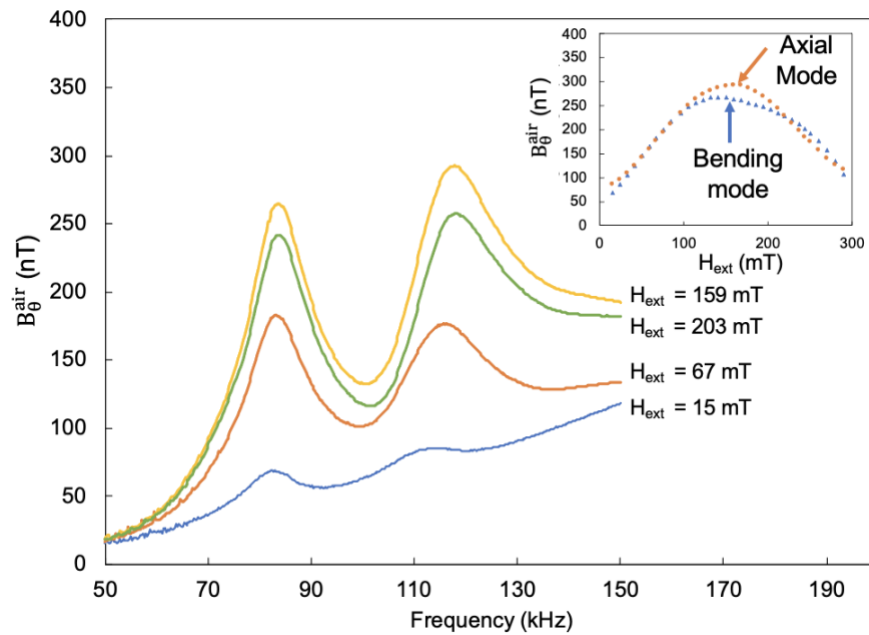

Figure 3.3 Measured transmitted magnetic fields versus frequency at three external bias fields. Upper right inset: measured signal versus external field

Figure 3.4 Figure 4 shows the radiation patterns, in units of nT, for the 83 kHz bending mode and 117 kHz axial mode measured at zero external magnetic bias (points) overlaid with analytical

radiation patterns (solid and dashed lines). Both measured datasets have two almost identical main lobes centered about 0° (probe orientation included in Figure 4) and 180° with different magnitudes. The bending mode has an emitted 27.96 nT signal and the axial mode has an emitted a 46.03 nT signal at 180°, showing a marked difference between the two frequencies because of the absence of an external bias, leading to larger influence by parasitics. The measured minima occur at 90° (probe orientation included in Figure 4) and 270°, however both patterns are skewed toward the 270° axis due to parasitic contributions from the PZT-8 wire leads. The dashed line corresponds to the computational model for the axial mode FDTD predicted magnetization change of $\Delta m_z = 9 \times 10^{-4}$. The FDTD predicted value of 110.79 nT at 180° is over two times larger than the measured axial mode radiation. The lower measured values are most likely due to magnetic pinning sites on the surface of the Galfenol slices resulting from heat affected zones (HAZ) created during the wire EDM cutting process (i.e. Δm_z decreases due to magnetization rotation resistance at pinning sites). The solid line show in in the Figure 4 is calculated using the dipole model curve fitted to the data producing a $\Delta m_z = 4 \times 10^{-4}$. These results provide confidence in the modeling approach and shows that the antenna acts as an infinitesimal dipole for both axial and bending modes despite it being electrically small (i.e. $\frac{\lambda}{8.8 \times 10^6}$).

The bottom inset of Figure 4 is a table listing B_θ^{air} measured as a function of distance (i.e. $3 < r < 10$ cm) at 130 mT applied bias field for the bending mode and axial mode, as well as the dipole predictions for the axial mode with $\Delta m_z = 4 \times 10^{-4}$ and $\Delta m_z = 9 \times 10^{-4}$. Both modes closely followed the theoretical $\frac{1}{r^3}$ dipole model decay trend with $\frac{1}{r^{3.15}}$ decay for the bending mode and $\frac{1}{r^{3.27}}$ decay for the axial mode. The two modes slowly converge to a similar emission strength at

10 cm, which is potentially attributed to the evolution of the signal produced from two different

magnetic moment distributions, i.e. bending vs axial.
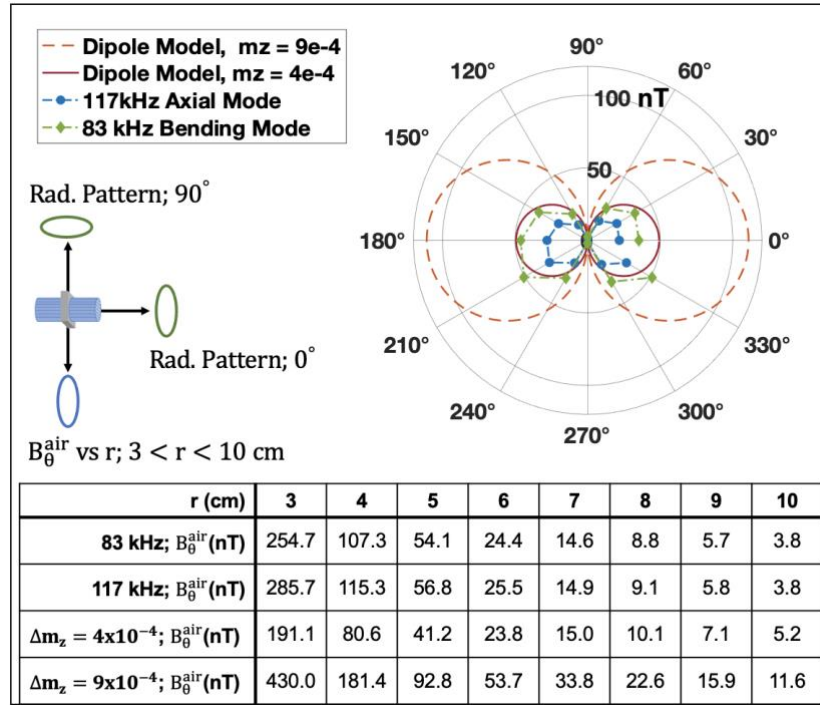
Figure 3.4 Measured radiation pattern for 83 kHz and 117 kHz modes; inset: table of measured

B_θ^{air} *vs distance at 83 kHz and 117 kHz modes with predicted values*

Figure 3.5 shows experimental data for the FSK communication demonstration with the proposed

dual band magnetoelectric antenna. Figure 5a shows normalized electric field E_{pzt}^* input versus

time, while Figure 5b shows the normalized magnetic signal received by the Langer probe, B_{air}^*,

versus time for the entire FSK sequence. During the FSK sequence, the frequency alternates

between 83 kHz to 117 kHz, with a representative dataset of 83 kHz highlighted in Figures 5a and

5b starting at 59.715 seconds and a representative dataset of 117 kHz highlighted in Figures 5a

and 5b starting at 69.725 seconds. These highlighted regions are shown in more detail as Figure

5d (83 kHz portion of modulated signal) and 5e (117 kHz portion of modulated signal) where E_{pzt}^* is plotted with a dashed line and B_{air}^* is plotted with a solid line. As seen when comparing Figures 5d and 5e, the received signal B_{air}^* frequency shifts with changing E_{pzt}^* frequency, but unlike E_{pzt}^*, the received B_{air}^* amplitude decreases ~2x as frequency changes from 117 kHz to 83 kHz. This is consistent with previously discussed measurements where the 83 kHz signal is consistently lower than 117 kHz signal due to the partial volume contribution to Δm_z seen in the bending mode as compared to the axial mode. Note that data shown in Figures 5d and 5e was obtained using an oscilloscope, which has a higher sampling rate as compared to the NI DAQ and the oscilloscope data was subsequently averaged to remove noise, leading to smoother B_{air}^* curves in Figures 5d and 5e when compared to Figure 5b. Figure 5c shows the digital bitstream for the entire FSK sequence, obtained from manual decoding of Figure 5b. The logical 0 portions of the bitstream correspond to the 83 kHz segments of the modulated FSK wave while the logical 1 portions of the bitstream correspond to the 117 kHz segments. When decoded into a digital message, the modulated wave is shown to communicate the word "HELLO."
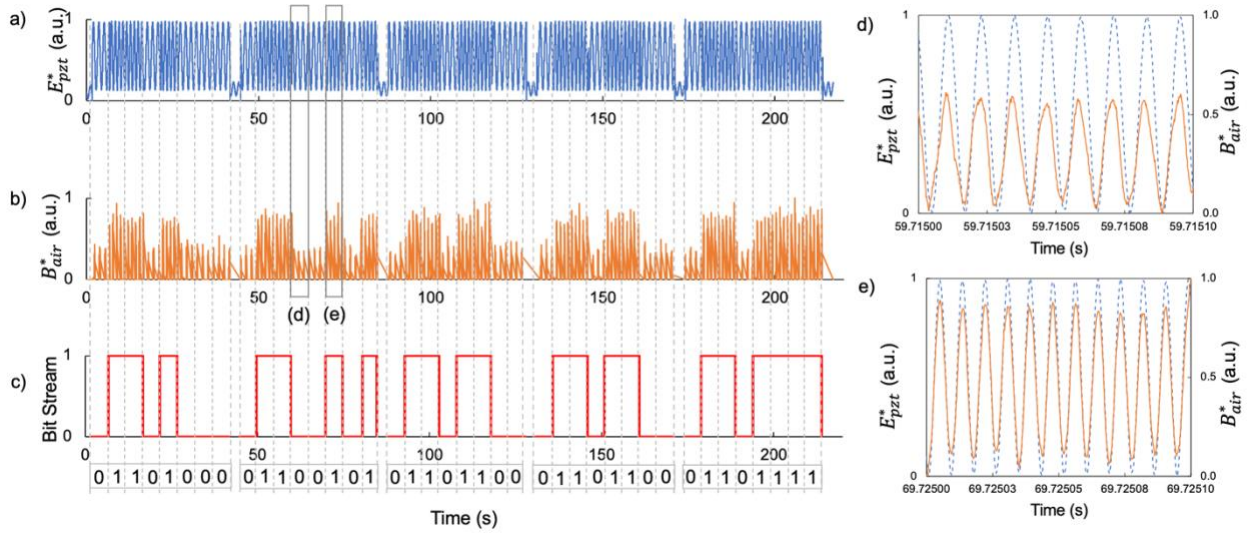
Figure 3.5 a) Digital bitstream; b) normalized input voltage to PZT-8; c) normalized transmitted signal; d) low frequency carrier wave; e) high frequency carrier wave

The bandwidth to operate this antenna in an on-off-keying (OOK) ASK communication scheme at the 83 kHz bending mode would be 21.4 kHz. However, the bandwidth of the system can be increased to 110.8 kHz by using FSK to switch between the 83 kHz and 117 kHz modes because of the 34 kHz separation between the two modes. The bandwidth can be increased even more, though, by using the other four modes present in the in the 30-200 kHz frequency range as shown in Figure 2b. Assuming that the carrier signal bandwidth remains the same, the total bandwidth could be increased to 320 kHz by using the 34.4 kHz and 173.3 kHz resonance modes for frequency shift keying. However, by utilizing the antenna's modes that are present outside of 30-200 kHz range, the total bandwidth could be increased even more, resulting in higher data transfer rates than previously possible with magnetoelectric antennas. Note that because continuous systems have infinite resonance frequencies [76], the signal can be keyed between the carrier frequency and even higher modes, dramatically increasing the bandwidth by increasing the spacing between carrier frequencies.

3.4 Conclusion

A dual band Galfenol/PZT-8 magnetoelectric antenna for near field FSK communication through lossy media was studied. The antenna consisted of two magnetostrictive Galfenol-polymer composites bonded to either side of a PZT-8 actuator to form a dumbbell orientation and resonate at both 83 kHz and 117 kHz. The antenna operates by applying an AC electric field to the PZT-8, inducing both an oscillating strain and magnetization in the magnetostrictive Galfenol blocks, yielding EM radiation in the near field. The antenna's impedance, quality factor, mechanical resonance, and radiation patterns were measured at both resonant frequencies as a function of bias magnetic field, frequency, and applied voltage. The measured data showed strong correlations to the simulation results, and discussions regarding parasitic signals were included. Finally, data transmission via FSK using the antenna's two resonant frequencies was demonstrated by sending a binary message, proving the efficacy of the dual band antenna for FSK communication.

Chapter 4: Dissertation Summary

Interest in communication through lossy media has garnered attention for magnetoelectric antennas in recent years. Magnetoelectric antennas radiate primarily magnetic energy in the near field by voltage induced strain driven magnetization oscillations. This magnetic energy does not interact with the conductive portions of lossy media, meaning that communication through the human body or sea water can be accomplished.

Chapter 2 focuses on an axial extension mode Metglas/PZT-5A magnetoelectric antenna. The radiated magnetic energy dominant electromagnetic waves at 88 kHz by applying an AC electric field to the piezoelectric, inducing both an oscillating strain and magnetization in the magnetostrictive Metglas block. This work presented a decoupled modelling system for predicting signal strengths in air using an analytical dipole model and a Landau-Lifshitz-Gilbert (LLG) micromagnetic model fed with strain predictions from finite element electromechanical simulations. The antenna was experimentally characterized as a function of bias magnetic field, frequency, and applied voltage. The measured data had strong correlation to the simulation results, representing a method for not just validating magnetoelectric antenna radiation, but also predicting it. Parametric studies were performed with other magnetostrictive materials (i.e. Galfenol and Terfenol-D) and an alternative piezoelectric actuator (i.e. PZT-8 instead of PZT-5A), determining that antennas with higher magnetostriction and Q factors could allow for device volume reduction up to 3 orders of magnitude.

Chapter 3 discussed a similar antenna to that of Chapter 2: an antenna consisting of two magnetostrictive Galfenol-polymer composites bonded to either side of a PZT-8 actuator to form

a dumbbell orientation and resonate at both 83 kHz and 117 kHz. Because this antenna resonates at two distinct frequencies, it is considered a dual band antenna and a wider range of communication schemes can be used to transmit data. Data transmission via frequency shift keying (FSK) using the antenna's two resonant frequencies was experimentally demonstrated and a binary message, 'hello', was successfully sent, thus proving the efficacy of the dual band magnetoelectric antenna for FSK communication. Using FSK on this dual band antenna dramatically increased the communication bandwidth, and the potential for further improvement is discussed.

References

[1]   Wadhawan, V. K. (2002). Ferroic materials: A primer. Resonance, 7(7), 15-24.

[2]   O'handley, R. C. (2000). Modern magnetic materials: principles and applications. Wiley.

[3]   Cullity, B. D., & Graham, C. D. (2011). *Introduction to magnetic materials*. John Wiley & Sons.

[4]   Kittel, C. (1949). Physical theory of ferromagnetic domains. *Reviews of modern Physics*, *21*(4), 541.

[5]   Williams, H. J., Bozorth, R. M., & Shockley, W. J. P. R. (1949). Magnetic domain patterns on single crystals of silicon iron. *Physical review*, *75*(1), 155.

[6]   Williams, H. J., & Shockley, W. (1949). A simple domain structure in an iron crystal showing a direct correlation with the magnetization. *Physical Review*, *75*(1), 178.

[7]   Wikipedia contributors. (2022, June 10). Vibrating-sample magnetometer. In *Wikipedia, The Free Encyclopedia*. Retrieved 23:10, May 31, 2022.

[8]   Vansteenkiste, A., Leliaert, J., Dvornik, M., Helsen, M., Garcia-Sanchez, F., & Van Waeyenberge, B. (2014). The design and verification of MuMax3. *AIP advances*, *4*(10), 107133.

[9]   Andò, B., Baglio, S., Bulsara, A. R., Caruso, V., In, V., & Sacco, V. (2006, April). Investigate the optimal geometry to minimize the demagnetizing effect in RTD-Fluxgate. In *2006 IEEE Instrumentation and Measurement Technology Conference Proceedings* (pp. 2175-2178). IEEE.

[10] Gilbert, T. L. (2004). A phenomenological theory of damping in ferromagnetic materials. *IEEE transactions on magnetics*, *40*(6), 3443-3449.

[11] Acosta, A., Fitzell, K., Schneider, J. D., Dong, C., Yao, Z., Sheil, R., ... & Chang, J. P. (2020). Underlayer effect on the soft magnetic, high frequency, and magnetostrictive properties of FeGa thin films. *Journal of Applied Physics*, *128*(1), 013903.

[12] Eerenstein, W., Mathur, N. D., & Scott, J. F. (2006). Multiferroic and magnetoelectric materials. *nature*, *442*(7104), 759-765.

[13] Dapino, M. J., Smith, R. C., & Flatau, A. B. (2000). Structural magnetic strain model for magnetostrictive transducers. *IEEE Transactions on magnetics*, *36*(3), 545-556.

[14] Lee, E. W. (1955). Magnetostriction and magnetomechanical effects. *Reports on progress in physics*, *18*(1), 184.

[15] Clark, A. E., Belson, H. S., & Tamagawa, N. (1973, January). Magnetocrystalline Anisotropy in Cubic Rare Earth-Fe2 Compounds. In *AIP Conference Proceedings* (Vol. 10, No. 1, pp. 749-753). American Institute of Physics.

[16] Clark, A. E., Restorff, J. B., Wun-Fogle, M., Lograsso, T. A., & Schlagel, D. L. (2000). Magnetostrictive properties of body-centered cubic Fe-Ga and Fe-Ga-Al alloys. *IEEE Transactions on Magnetics*, *36*(5), 3238-3240.

[17] Jaffe, H., & Berlincourt, D. A. (1965). Piezoelectric transducer materials. *Proceedings of the IEEE*, *53*(10), 1372-1386.

[18] Klooster, V. (1959). Three centuries of Rochelle salt. *Journal of chemical education*, *36*(7), 314.

[19] Hill, N. A. (2000). Why are there so few magnetic ferroelectrics?. *The journal of physical chemistry B*, *104*(29), 6694-6709.

[20] Schmid, H. (1994). Multi-ferroic magnetoelectrics. *Ferroelectrics*, *162*(1), 317-338.

[21] Lottermoser, T., & Meier, D. (2021). A short history of multiferroics. *Physical Sciences Reviews*, *6*(2).

[22] Eerenstein, W., Mathur, N. D., & Scott, J. F. (2006). Multiferroic and magnetoelectric materials. *nature*, *442*(7104), 759-765.

[23] Spaldin, N. A., & Fiebig, M. (2005). The renaissance of magnetoelectric multiferroics. *Science*, *309*(5733), 391-392.

[24] Nan, C. W., Bichurin, M. I., Dong, S., Viehland, D., & Srinivasan, G. (2008). Multiferroic magnetoelectric composites: Historical perspective, status, and future directions. *Journal of applied physics*, *103*(3), 1.

[25] Balanis, C. A. (2015). *Antenna theory: analysis and design*. John wiley & sons.

[26] Kraus, J. D. (1988). Heinrich Hertz-theorist and experimenter. *IEEE Transactions on Microwave Theory and Techniques*, *36*(5), 824-829.

[27] Chu, L. J. (1948). Physical limitations of omni-directional antennas. *Journal of applied physics*, *19*(12), 1163-1175.

[28] Xu, X., & Wang, Y. E. (2007, March). Chu's Limit and Switched Electrically Small Antennas. In *2007 International workshop on Antenna Technology: Small and Smart Antennas Metamaterials and Applications* (pp. 463-466). IEEE.

[29] Tiwari, S. (2020). *Dynamics of Multiferroic Coupling*. University of California, Los Angeles.

[30] Fowler, C. M., Garn, W. B., & Caird, R. S. (1960). Production of very high magnetic fields by implosion. *Journal of Applied Physics*, *31*(3), 588-594.

[31] *Sonar - historical development of sonar*. Historical Development Of Sonar - Sound, Detection, Systems, and Devices - JRank Articles. (n.d.). Retrieved August 8, 2022, from https://science.jrank.org/pages/6289/SONAR-Historical-development-SONAR.html

[32] Calkins, F. T., Smith, R. C., & Flatau, A. B. (2000). Energy-based hysteresis model for magnetostrictive transducers. *IEEE Transactions on Magnetics*, *36*(2), 429-439.

[33] Dapino, M. J., Smith, R. C., & Flatau, A. B. (2000). Structural magnetic strain model for magnetostrictive transducers. *IEEE Transactions on magnetics*, *36*(3), 545-556.

[34] Dong, S., Li, J. F., & Viehland, D. (2004). Vortex magnetic field sensor based on ring-type magnetoelectric laminate. *Applied physics letters*, *85*(12), 2307-2309.

[35] Bichurin, M. I., Kornev, I. A., Petrov, V. M., Tatarenko, A. S., Kiliba, Y. V., & Srinivasan, G. (2001). Theory of magnetoelectric effects at microwave frequencies in a piezoelectric/magnetostrictive multilayer composite. *Physical Review B*, *64*(9), 094409.

[36] R. J. Miller, W. P. Geren, and S. P. Hubbell, "Multiferroic antenna/sensor," U.S. Patent 20 110 062 955, Mar. 17, 2011

[37] Nan, T., Hui, Y., Rinaldi, M., & Sun, N. X. (2013). Self-biased 215MHz magnetoelectric NEMS resonator for ultra-sensitive DC magnetic field detection. *Scientific reports*, *3*(1), 1-6.

[38] Lin, H., Nan, T., Qian, Z., Gao, Y., Hui, Y., Wang, X., ... & Sun, N. X. (2016, May). Tunable RF band-pass filters based on NEMS magnetoelectric resonators. In *2016 IEEE MTT-S International Microwave Symposium (IMS)* (pp. 1-4). IEEE.

[39] Nan, T., Lin, H., Gao, Y., Matyushov, A., Yu, G., Chen, H., ... & Sun, N. X. (2017). Acoustically actuated ultra-compact NEMS magnetoelectric antennas. *Nature communications*, *8*(1), 1-8.

[40] Liang, X., Chen, H., Sun, N., Gao, Y., Lin, H., & Sun, N. X. (2020, July). Mechanically driven SMR-based MEMS magnetoelectric antennas. In *2020 IEEE International*

Symposium on Antennas and Propagation and North American Radio Science Meeting (pp. 661-662). IEEE.

[41] Yao, Z., Tiwari, S., Lu, T., Rivera, J., Luong, K. Q., Candler, R. N., ... & Wang, Y. E. (2019). Modeling of multiple dynamics in the radiation of bulk acoustic wave antennas. *IEEE Journal on Multiscale and Multiphysics Computational Techniques*, *5*, 5-18.

[42] Yao, Z. (2017). A Multiscale, Unconditionally Stable Multiphysics Time-Domain (MUST) Solver Unifying Electrodynamics, Elastodynamics and Spin Dynamics. *UCLA*. ProQuest ID: Yao_ucla_0031D_16328. Merritt ID: ark:/13030/m5b32r28. Retrieved from https://escholarship.org/uc/item/2b39p643

[43] Xu, J., Leung, C. M., Zhuang, X., Li, J., Bhardwaj, S., Volakis, J., & Viehland, D. (2019). A low frequency mechanical transmitter based on magnetoelectric heterostructures operated at their resonance frequency. *Sensors*, *19*(4), 853.

[44] Kemp, M. A., Franzi, M., Haase, A., Jongewaard, E., Whittaker, M. T., Kirkpatrick, M., & Sparr, R. (2019). A high Q piezoelectric resonator as a portable VLF transmitter. *Nature communications*, *10*(1), 1-7.

[45] Schneider, J. D., Domann, J. P., Panduranga, M. K., Tiwari, S., Shirazi, P., Yao, Z., ... & Carman, G. P. (2019). Experimental demonstration and operating principles of a multiferroic antenna. *Journal of applied physics*, *126*(22), 224104.

[46] Manteghi, M., & Ibraheem, A. A. Y. (2014). On the study of the near-fields of electric and magnetic small antennas in lossy media. *IEEE Transactions on antennas and propagation*, *62*(12), 6491-6495.

[47] Shahan, D. (2020, January 28-29). *VIBRational ANTennas (Vibrant) for Long Wave Applications*. [Conference presentation]. TANMS Annual Research Strategy Meeting. Los Angeles, CA, USA.

[48] Niu, Y., & Ren, H. (2021). Transceiving signals by mechanical resonance: A low frequency (LF) magnetoelectric mechanical antenna pair with integrated DC magnetic bias. *arXiv preprint arXiv:2107.13295*.

[49] Vaillancourt, P., Djemouai, A., Harvey, J. F., & Sawan, M. (1997, October). EM radiation behavior upon biological tissues in a radio-frequency power transfer link for a cortical visual implant. In *Proceedings of the 19th Annual International Conference of the IEEE Engineering in Medicine and Biology Society.'Magnificent Milestones and Emerging Opportunities in Medical Engineering'(Cat. No. 97CH36136)* (Vol. 6, pp. 2499-2502). IEEE.

[50] Bian, S., Zhu, B., Rong, G., & Sawan, M. (2021). Towards wearable and implantable continuous drug monitoring: A review. *Journal of pharmaceutical analysis*, *11*(1), 1-14.

[51] Scanlon, W. G., Evans, N. E., & McCreesh, Z. M. (1997). RF performance of a 418-MHz radio telemeter packaged for human vaginal placement. *IEEE transactions on biomedical engineering*, *44*(5), 427-430.

[52] Soontornpipit, P., Furse, C. M., & Chung, Y. C. (2004). Design of implantable microstrip antenna for communication with medical implants. *IEEE Transactions on Microwave theory and techniques*, *52*(8), 1944-1951.

[53] Furse, C. M., & Chrysler, A. (2014, July). A history & future of implantable antennas. In *2014 IEEE Antennas and Propagation Society International Symposium (APSURSI)* (pp. 527-528). IEEE.

[54] International Commission on Non-Ionizing Radiation Protection. (2020). Guidelines for limiting exposure to electromagnetic fields (100 kHz to 300 GHz). *Health physics*, *118*(5), 483-524.

[55] Bailey, W. H., Bodemann, R., Bushberg, J., Chou, C. K., Cleveland, R., Faraone, A., ... & Zollman, P. M. (2019). Synopsis of IEEE Std C95. 1™-2019 "IEEE Standard for Safety Levels With Respect to Human Exposure to Electric, Magnetic, and Electromagnetic Fields, 0 Hz to 300 GHz". *IEEE Access*, *7*, 171346-171356.

[56] Ben Amar, A., Kouki, A. B., & Cao, H. (2015). Power approaches for implantable medical devices. *sensors*, *15*(11), 28889-28914.

[57] Dea, J., Radosevic, D., Tran, N., Chavez, J., & Neuner III, B. (2017). *Land and undersea field testing of very low frequency rf antennas and loop transceivers*. SSC Pacific San Diego United States.

[58] O'Handley, R. C., Huang, J. K., Bono, D. C., & Simon, J. (2008). Improved wireless, transcutaneous power transmission for in vivo applications. *IEEE Sensors Journal*, *8*(1), 57-62.

[59] Saha, O., Andersen, E., & Roundy, S. (2021, December). Wireless Power Transfer by Self-biased Magnetoelectric Laminate for Biomedical Implants. In *2021 IEEE 20th International Conference on Micro and Nanotechnology for Power Generation and Energy Conversion Applications (PowerMEMS)* (pp. 36-39). IEEE.

[60] Medtronic. (n.d.). *Micra pacemakers - transcatheter pacing systems*. Medtronic. Retrieved August 16, 2022, from https://www.medtronic.com/us-en/healthcare-professionals/products/cardiac-rhythm/pacemakers/micra-pacing-system.html

[61] The New York Times. (2021, October 4). *A 'pacemaker for the brain': No treatment helped her depression - until this*. The New York Times. Retrieved October 6, 2021, from https://www.nytimes.com/2021/10/04/health/depression-treatment-deep-brain-stimulation.html

[62] Bonner, M. D., Greenhut, S. E., Sheldon, T. J., & Demmer, W. M. (2016, June 28). Leadless Pacemaker System.

[63] Kim, H. J., Hirayama, H., Kim, S., Han, K. J., Zhang, R., & Choi, J. W. (2017). Review of near-field wireless power and communication for biomedical applications. IEEE Access, 5, 21264-21285.

[64] Domann, J. P., & Carman, G. P. (2017). Strain powered antennas. Journal of Applied Physics, 121(4).

[65] Hashimoto, K. Y. (2009). RF bulk acoustic wave filters for communications. Artech House.

[66] Mukherjee, D., & Mallick, D. (2023). A self-biased, low-frequency, miniaturized magnetoelectric antenna for implantable medical device applications. Applied Physics Letters, 122(1).

[67] Dong, C., He, Y., Li, M., Tu, C., Chu, Z., Liang, X., ... & Sun, N. X. (2020). A portable very low frequency (VLF) communication system based on acoustically actuated magnetoelectric antennas. IEEE Antennas and Wireless Propagation Letters, 19(3), 398-402.

[68] Du, Y., Xu, Y., Wu, J., Qiao, J., Wang, Z., Hu, Z., ... & Liu, M. (2023). Very-Low-Frequency Magnetoelectric Antennas for Portable Underwater Communication: Theory and Experiment. IEEE Transactions on Antennas and Propagation, 71(3), 2167-2181.

[69] Or, S. W., Nersessian, N., & Carman, G. P. (2004). Dynamic magnetomechanical behavior of Terfenol-D/epoxy 1-3 particulate composites. IEEE transactions on magnetics, 40(1), 71-77.

[70] Ulaby, F. T., & Ravaioli, U. (2020). Fundamentals of Applied Electromagnetics. (8 ed.) Pearson.

[71] Uchino, K. (1998). Piezoelectric ultrasonic motors: overview. Smart materials and structures, 7(3), 273.

[72] Aharoni, A. (1998). Demagnetizing factors for rectangular ferromagnetic prisms. Journal of applied physics, 83(6), 3432-3434.

[73] Gollakota, S., Hassanieh, H., Ransford, B., Katabi, D., & Fu, K. (2011, August). They can hear your heartbeats: Non-invasive security for implantable medical devices. In Proceedings of the ACM SIGCOMM 2011 conference (pp. 2-13).

[74] Pozar, David M. (2012). Microwave engineering. Hoboken, NJ :Wiley.

[75] Burnside, E., Tiwari, S., Burnside, S., Candler, R., Henderson, R., Grimm, S., Carman, G. (2023). An Axial Mode Magnetoelectric Antenna: Radiation Predictions via Multiphysics Modeling with Experimental Validations. [Manuscript submitted for publication].

[76] Rao, S. (2007) Vibration of Continuous Systems. Wiley, Hoboken.